IEEE Access
Multidisciplinary | Rapid Review | Open Access Journal

Received June 27, 2021, accepted July 28, 2021, date of publication August 5, 2021, date of current version August 18, 2021.

Digital Object Identifier 10.1109/ACCESS.2021.3102829

Overview of Frequency-Control Technologies for a VSC-HVDC-Integrated Wind Farm

CHUNG-HAN LIN AND YUAN-KANG WU, (Member, IEEE)
Department of Electrical Engineering, National Chung-Cheng University, Minxiong, Chiayi 62102, Taiwan
Corresponding author: Yuan-Kang Wu (allenwu@ccu.edu.tw)

This work was supported by the Ministry of Science and Technology (MOST) of Taiwan under Grant MSOT 109-2221-E-194-005.

ABSTRACT In modern power systems, the increasing penetration of renewable energy resources has reduced the overall system inertia. However, the intermittent nature of wind power generation reduces frequency stability, which is a crucial issue. Consequently, modern power systems require that renewable energy sources, such as offshore wind farms, support the frequency regulation. High voltage direct current (HVDC) systems based on voltage source converters (VSCs) are currently being used to connect wind farms with the main grid. By adjusting the DC-link voltage of the VSC-HVDC, a capacitor can absorb or release energy to provide frequency support. In addition, the VSC-HVDC system can coordinate wind farms to support frequency regulation and thereby achieve better performance. Thus, this paper reviews and compares various frequency-control strategies for a VSC-HVDC-connected wind farm. This work implements in PSCAD/EMTDC a simulation of typical frequency-control techniques to verify their effectiveness and robustness. Furthermore, this paper shows the advantages and drawbacks of each frequency regulation method. Other auxiliary services for supporting frequency regulation, such as by energy storage systems, are also discussed. Finally, this paper provides complete recommendations for frequency regulation techniques for VSC-HVDC-integrated wind farms.

INDEX TERMS Renewable energy, inertia, energy storage system, frequency regulation, offshore wind farm, VSC-HVDC.

ABBREVIATIONS

AFR	Adaptive Frequency Regulation
AGC	Automatic Generation Control
AI	Artificial Intelligence
BESS	Battery Energy Storage System
DFIG	Doubly-Fed Induction Generator
EMF	Electromotive Force
ESS	Energy Storage System
FESS	Flywheel Energy Storage System
FR	Frequency Regulation
GEC	Generator Emulation Control
GSVSC	Grid-Side Voltage Source Converter
HESS	Hybrid Energy Storage System
HVDC	High-Voltage Direct-Current
IEC	Inertia Emulation Control
IR	Inertial Response
KE	Kinetic Energy
LCC	Line Commutated Converter-based
MPC	Model Predictive Control
MPPT	Maximum Power Point Tracking
MTDC	Multi-Terminal HVDC
OWF	Offshore Wind Farm
PCC	Point of Common Coupling
PFR	Primary Frequency Response
PI	Proportional Integral
PLL	Phase Locked Loop
PWM	Pulse Width Modulation
RES	Renewable Energy Sources
ROCOF	Rate of Change of Frequency
SC	Supercapacitor
SCADA	Supervisory Control And Data Acquisition
SCR	Short-Circuit Ratio
SFD	Second Frequency Drop
SFR	Second Frequency Response
SG	Synchronous Generator
SMES	Superconducting Magnetic Energy Storage
SOC	State of Charge

The associate editor coordinating the review of this manuscript and approving it for publication was Ali Raza.

TFR	Tertiary Frequency Response
TSR	Tip Speed Ratio
VSC	Voltage Source Converter
VSG	Virtual Synchronous Generator
VSM	Virtual Synchronous Machine
WF	Wind Farm
WFVSC	Wind-Farm-side Voltage Source Converter
WT	Wind Turbine

SYMBOLS

P_{wind}	Mechanical energy captured from wind
ρ	Air density
R	Radius of the wind rotor blade
V_w	Wind Speed
C_P	Power coefficient
λ	Tip Speed Ratio
β	Pitch angle
ω_t	Rotational speed of the blade
P^*_{WT}, P_{WT}	Reference and actual electrical power of the wind turbine
H_D	Inertia constant of the DFIG
K_i	Integral gain
K_p	Proportional gain
β_{max}	Maximum value of the pitch angle
β_{min}	Minimum value of the pitch angle
T_d	Time constant of the pitch angle controller
P_{del}	Reference active power of the deloaded WT
P_{opt}	Optimal reference active power of the WT
x	Power margin of the deloaded WT in %.
$C_{p,del}$	Power coefficient of the deloaded wind turbine
f	Frequency
f_0	Nominal frequency
Δf	Deviation of frequency
f^*_{WF}, f_{WF}	Reference and actual WFVSC frequency
f_{WF0}	Nominal WFVSC frequency
Δf_{WF}	Deviation of WFVSC frequency
K_{in}	Gain for the inertial response of WT
P_{in}	Active power due to the IR
P_f	Active power due to the droop control
R	Droop constant
v_d, v_q	Voltages in dq reference frame
i_d, i_q	Currents in dq reference frame
i^*_d, i^*_q	Reference currents in in dq reference frame
V^*_{DC}, V_{DC}	Reference and actual DC-link voltages
V_{DC0}	Nominal value of the DC-link voltage
$V_{DC,max}$	Maximum value of the DC-link voltage
$V_{DC,min}$	Minimum value of the DC-link voltage
ΔV_{DC}	Deviation of the DC-link voltage
ΔV^*_{DC}	Reference deviation of the DC-link voltage
V^*_{rms}, V_{rms}	Reference and actual AC voltages in root-mean-square
P^*, P	Reference and actual active power
Q^*, Q	Reference and actual reactive power
v_{cd}, v_{cq}	Actual output voltages of the converter of the VSC-HVDC in dq reference frame
v^*_{cd}, v^*_{cq}	Reference output voltages of the converter of the VSC-HVDC in dq reference frame
v_{sd}, v_{sq}	Actual grid side voltages in dq reference frame.
v^*_{sd}, v^*_{sq}	Reference grid side voltages in dq reference frame.
i_{sd}, i_{sq}	Actual grid side currents in dq reference frame.
i^*_{sd}, i^*_{sq}	Reference grid side currents in dq reference frame.
R, L	Equivalent resistance and inductance of the line.
ω	Angular frequency
W_c	Energy stored in the DC-link capacitors
C	Equivalent DC-link capacitance
P_C	Active power of the DC-link capacitors
K_A, K_B	Multipliers for the $f - V_{DC}$ and $V_{DC} - f_{WF}$ droop characteristics
H	Inertia constant of the SG
E_K	Stored kinetic energy of the SG
E_e	Electromagnetic energy stored in the DC-link capacitors
N	The total number of capacitors installed in the DC-link
H_{VSC}	Inertia constant of VSC-HVDC for the IEC
S_{VSC}	Converter capacity of VSC-HVDC
P_{in}, P_{out}	Input and output active powers of GSVSC toward the grid
P^*_H	Reference active power of GSVSC for IEC
τ	Designed time constant for the IEC
s	Complex frequency
P^*_{WF}	Reference active power for WF
K_{WF}	Multiplier for the $V_{DC} - P_{WF}$ droop of IEC
V_{WF}	AC voltage of the WFVSC
m_a	Amplitude modulation index for PWM
V^*_{DCf}	Reference DC-link voltage of the ancillary DC-link voltage controller
T_{DC}	Time constant of the ancillary DC-link voltage controller
E	Internal EMF of the SG
X	Equivalent reactance of the SG
V_o	Terminal voltage of the SG
δ	Difference of phase angle between E and V_o
P_o	Output active power of the SG
ω_{gen}	Electrical angular frequency of the EMF
ω_{grid}	Electrical angular frequency of the grid voltage
k_s	Equaling to $\lvert V_o \rvert \lvert V_{gen} \rvert / X$
k_g	The gain related to the number of poles and the moment of inertia
k_d	The gain related to the droop constant
k_o	The output gain of the GEC controller
P_0, Q_0	Initial active power and initial reactive power
E_0	No load electromotive force
D_p	Damping coefficient

D_q Reactive power coefficient
K_U Voltage coefficient for VSG

I. INTRODUCTION

Modern power systems are facing a succession of challenges of frequency stability, owing to the increasing penetration of wind energy [1]. Unlike conventional synchronous generators (SGs), wind turbines (WTs) cannot naturally provide frequency support to a power system. This is because the output power of wind farms (WFs) is decoupled from the system frequency, owing to the AC/DC/AC converters [2].

If load shedding or an SG outage occurs in a power system, then the power system frequency will deviate from its nominal value because of the power imbalance between the supply and demand. A large overall system inertia can help to stabilize the frequency. Therefore, there have been many studies to increase inertia from renewable energy. The frequency support techniques for WTs have been addressed in [3]–[7], which include inertial control, static/dynamic droop control, stepwise inertial control, fast power reserve and so on. The authors in [3] analyzed the energy stored in the rotating mass of WTs. They compared two different control methods based on changing the reference value of WT's torque for providing inertia response. In [4], the control of the electrical torque and the output power of a WT were studied and compared. The controller was based on the time derivative of the frequency, so as to provide an inertia response.

Voltage source converter based High Voltage Direct Current (VSC-HVDC) transmission systems are seen as a solution to connect offshore wind farms (OWFs) with onshore grids. Although the costs of the converters are high, a longer transmission distance will lead to a lower overall investment cost [8]. As a result, the number of cases for VSC-HVDC-connected OWFs has been increasing in recent years. However, similar to other conventional converters, the converters of the VSC-HVDC systems also decouple the available wind generation from the system frequency. The decoupled characteristics of the grid frequency f, the DC-link voltage V_{DC} and the WF's side frequency f_{WF} are depicted in Fig. 1 where V_{DC} and f_{WF} remain constant irrespective of the f value.

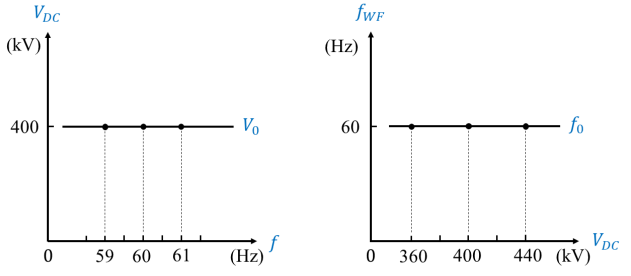

FIGURE 1. The decoupled characteristics of the grid frequency, DC-link voltage and the wind farm side frequency for a VSC-HVDC system.

Energy storage systems (ESSs) play a prominent role in the power systems. The numerous benefits of ESSs for wind power applications were summarized in [9]. For instance, fault ride through, power fluctuation mitigation, and spinning reserves are common services provided by ESSs. An ESS can participate in frequency regulation (FR) control and can collaborate with the WF to improve the overall system inertia [10]–[17]. Furthermore, for a further specific application in FR, the ESS can coordinate with the WF to prevent a second frequency drop (SFD) during the recovery of generator rotor speed of WTs [17].

Some review papers have organized several frequency control techniques for WTs [17]–[22]. The authors in [23] discussed the limitations of frequency support techniques for WTs and advised that the maximum power point tracking (MPPT) algorithm, minimum operating rotor speed, and nonlinearities and optimization of the frequency support be further investigated. Reference [24] reviewed the design of multiple controllers for primary and secondary frequency control for WTs.

A DC-based wind farm (WF) is viewed as a prominent and cost-effective topology for the commercial wind industry. As wind turbines (WTs) are connected to a single DC-bus, the number of DC/AC inverters and transformers can be greatly reduced. The grid connection of a DC-based WF should be worthy of attention. The influences of DC-based WFs on the AC grid during a dynamic situation and fault ride-through characteristic were investigated in [25]. Furthermore, a resonance circuit between HVDC and DC-based WFs may cause a severe oscillation when AC voltage variations or power imbalances occur in AC grids. The authors in [26] analyzed the impacts of different DC line models on the resonance phenomenon in a DC-based WF.

Several studies discussed the frequency control strategies for all-DC WFs. The authors in [27] investigated active and reactive power controls for a medium voltage DC (MVDC)-connected WF. The proposed topology contains ultra-capacitors and battery storage systems for supporting AC voltage control and frequency droop control. Reference [28] proposed a communication-free approach for all-DC OWFs for providing frequency support. The communication-free approach can regulate the voltage at onshore or offshore converters according to frequency deviation. Therefore, the OWF can participate in the frequency regulation scheme by monitoring the DC voltage at the offshore converter. Furthermore, the time delay due to the communication channel can be avoided by using ancillary voltage controllers. The authors in [29] proposed a coordinated frequency control strategy called inertia synchronizing control for all-DC WFs. The all-DC WF is connected to the onshore converter through MVDC and HVDC lines. The converter at the WF side can automatically synchronize with AC grid without phase-locked-loop (PLL). The DC-bus voltage is firstly controlled by the grid-side converter. Afterwards, the DC capacitors and the all-DC WF can provide frequency support according to the voltage variation at the DC bus. Particularly, the control method can be applied to weak grids. In [30], a DC collection was adopted for collecting the output power of WTs, and these WTs can provide voltage and

frequency supports based on the DC-bus voltage. The grid-side converter was designed as a virtual synchronous generator to support inertia. By contrast, the WF-side converters deploy the power-voltage droop characteristics to distribute power flows. In summary, these aforementioned frequency control strategies for all-DC WFs rely mainly on the DC-bus voltage as a medium for transmitting the disturbance of grid frequency to a WF, which enables WTs to participate in frequency regulation.

Among articles giving overviews of FR techniques for the VSC-HVDC, reference [31] introduced some coordinated FR strategies by means of discussion, but does not include the control diagrams of these methods. Reference [32] summarized the inertial control, droop control, proportional integral (PI)-based control, and their modified controllers for FR in a VSC-HVDC system. The authors in [33] proposed a classification of inertia control strategies for the VSC-HVDC based on the type of synchronization with the grid and the coordination between other generation sources: synchronized with and without phase-locked-loop (PLL), centralized control, and distributed control. Reference [34] reviewed the numerous existing control strategies, e.g., SG-based, swing-equation-based, and droop-based topologies for the inverter to provide virtual inertia support. Nonetheless, these studies did not consider the dynamic behaviors of the WF in the FR structure.

Among these studies, none gave a comprehensive overview of control strategies for coordinating the VSC-HVDC and the WF for participating in an FR scheme. However, how to integrate VSC-HVDC in a WF is a current research trend and cooperation between the VSC-HVDC and WF should be further studied. Hence, this study summarizes existing FR strategies for VSC-HVDC-connected WFs. The contributions of this work are as follows:

1) Analyzes of the pros and cons of each technique and comprehensive comparisons.
2) Detailed designs of the FR controllers for VSC-HVDC-integrated WFs.
3) In particular, several time-domain simulation cases for selected control strategies.
4) Studies of coordinated FR techniques for WFs and ESSs
5) Illustration of the challenges and difficulties of existing FR techniques, providing future solutions and recommendations.

The rest of this paper is organized as follows. Section II introduces the basic operation theorems of the WTs and the VSC-HVDC system. Section III describes the various frequency-control strategies for VSC-HVDC-integrated WFs and the design of the controllers. Simulation results and a comprehensive comparison of different FR strategies for a VSC-HVDC-connected WF are presented in Section IV. Next, the FR strategies for WTs and ESSs are introduced in Section V. The future research trends are presented in Section VI. Finally, the conclusions are drawn in Section VII.

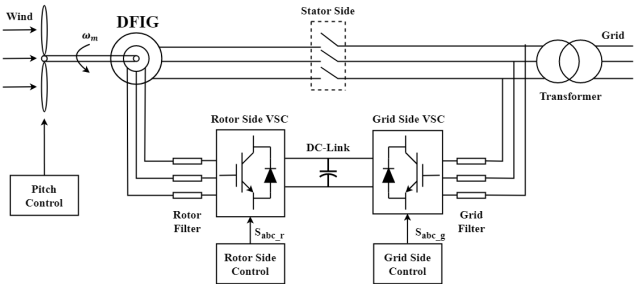

FIGURE 2. The schematic diagram of DFIG-based WT system.

II. BASIC THEOREMS OF WIND TURBINES AND VSC-HVDC

A. AERODYNAMICS OF WIND TURBINES

The doubly-fed induction generator (DFIG) is selected as the type of WT to be studied. The structure of the DFIG is shown in Fig. 2. The mechanical energy captured from wind, P_{wind}, can be expressed [35] as:

$$P_{wind} = \frac{1}{2}\rho\pi R^2 V_w^3 C_p(\lambda, \beta) \tag{1}$$

where ρ is the air density; R is the radius of the rotor blade; V_w is the wind speed and C_p is the power coefficient, which is a function of tip speed ratio (TSR), λ, and the pitch angle, β. The definition of λ is:

$$\lambda = \frac{\omega_t \cdot R}{V_w} \tag{2}$$

where ω_t is the rotational speed of the blade.

The active power generated by the DFIG is controlled by the MPPT algorithm. The reference value of active power is set according to wind speed and rotor speed. By using the MPPT algorithm, the DFIG can operate on an optimal power curve for various wind speeds. The relationship between the mechanical power and the electrical power, P_{WT}, of the DFIG is expressed as:

$$2H_D \cdot \overline{\omega_t} \cdot \frac{d\overline{\omega_t}}{dt} = \overline{P_{wind}} - \overline{P_{WT}} \tag{3}$$

where H_D is the inertia constant of the DFIG; ω_t is the rotational speed of the DFIG and the upper bar represents the per-unit value. Equation (3) is the well-known swing equation.

B. DELOADING METHODS OF WIND TURBINES

By using the MPPT algorithm, the WTs can capture maximum power from the wind to maintain a high level of wind energy harvesting. However, operating at the optimal point indicates that there is no additional power reserve for the WTs to provide frequency support. If the WTs need to release the kinetic energy stored in the rotor back to the grid, then the rotor speed must be reduced and the extra energy must be absorbed by the WTs during rotor speed recovery, which requires another control strategy. To provide reserve

power for frequency support, there are two common deloading methods [36]: pitch angle control and the overspeeding technique.

In general, the pitch angle is zero in low wind-speed conditions. When the wind speed exceeds the rated wind speed, the WT will operate at full load. Meanwhile, the rotational speed should be limited to the rated speed to protect the rotor and the equipment; this is done by activating the pitch angle controller. The control diagram of the pitch angle controller is shown in Fig. 3.

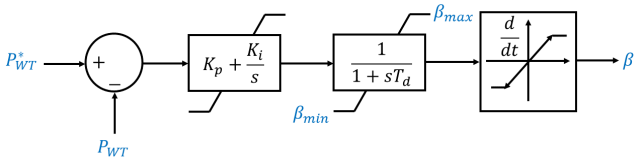

FIGURE 3. The pitch angle controller.

The mainstream PI controller is utilized for pitch angle control. The reference power, P^*_{WT}, is the deloaded signal according to the desired power margin and P_{WT} is the measured WT power. The difference between them is passed through a PI controller, a first-order transfer function and the rate limiter, in order to obtain the pitch angle. The time constant T_d is often related to the time delay. The upper limit β_{max} and the lower limit β_{min} are set to be 27° and −27°, respectively. The rate of change of the pitch angle is limited within ±10°/s to prevent a sudden variation.

Fig. 4 shows the output power of a WT under different wind speeds. The red curve represents the MPPT curve, e.g., point A is the optimal point at a wind speed of 9 m/s. The operating point of the WT can be shifted to the right or the left of the optimal power point to change the TSR, and thus the deloading operation based on speed control can be achieved, as presented in Fig. 4. The overspeeding technique is preferred because the kinetic energy stored in the rotor mass can be released to the grid, when the WT increases its output power from point B towards point A. It is noted that, in a low wind-speed range, only the overspeeding technique

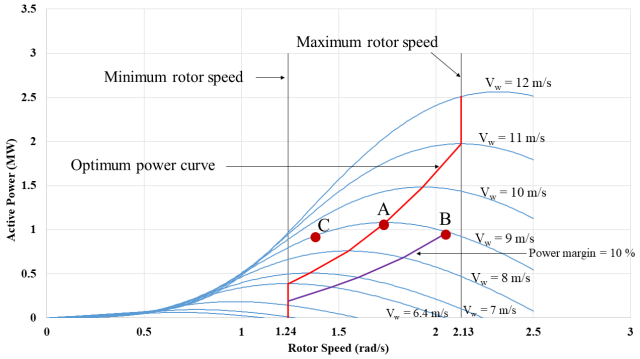

FIGURE 4. Active power – rotor speed curves under different wind speeds. Red curve and purple curve represent the MPPT curve and the deloaded curve for 10% power margin, respectively.

can be applied. In a medium wind-speed range, the pitch angle control and overspeeding technique can be activated simultaneously. Finally, in a high wind-speed range, the pitch angle controller plays a crucial role in limiting the maximum output power of the WT since the overspeeding technique causes the WT to exceed its rating.

The desired power margin, x, decides the deloaded reference power as:

$$P_{del} = P_{opt}\,(1 - x) \tag{4}$$

where P_{opt} is the optimal power reference. Hence, the target operating points lie on the sub-optimal power curve instead of the MPPT curve. Once the sub-optimal point is obtained, the corresponding power coefficient, $C_{p,del}$, can be determined as:

$$C_{p,del} = \frac{P_{opt}\,(1 - x)}{\frac{1}{2}\rho\pi R^2 V_w^3} = C_{p,del}\,(V_w, \omega_t, \beta) \tag{5}$$

Hence, for a given pitch angle and wind speed, the rotor speed corresponding to the sub-optimal curve can be obtained. Then the deloaded power can be calculated according to (4) and (5).

C. FREQUENCY REGULATION CAPABILITY OF WIND TURBINES

In general, the process of FR after a sudden imbalance of the power flow can be divided into four different successive steps: inertial response (IR), primary frequency response (PFR), secondary frequency response (SFR) and tertiary frequency response (TFR) [37]–[39]. SFR is usually called as automatic generation control (AGC) [7]. Fig. 5 (a) shows the frequency response for a low-frequency event. The IR is immediately activated when detecting a generator trip-off or a load increase, and it lasts for a few seconds. The purpose of IR is to reduce the rate of change of frequency (ROCOF) and to increase the frequency nadir. The PFR related to droop control owing to the SG governor should start within a few seconds and be fully deployed by 30 s. It is noted that the PFR often contributes to a temporary steady state where the grid system is stabilized at a specific value [40]. Subsequently, the SFR is deployed from 30 s to 15 min to bring the frequency back to the nominal value and to free the PFR. Finally, the system operators manually use the TFR to free the previous reserves [41], [42]. A schematic diagram of the successive power reserves is depicted in Fig. 5(b).

Renewable energy sources such as solar and wind do not possess inertia. However, by utilizing synthetic or virtual inertia techniques, WTs are capable of similar inertia response behaviors as conventional SGs. This study summarizes two common control schemes [43], [44].

According to the method proposed in [3], the aim of inertial control is to mimic the inertial response of a conventional SG. When the system frequency drops, the kinetic energy stored in the rotating mass of the WT is released to the grid. The

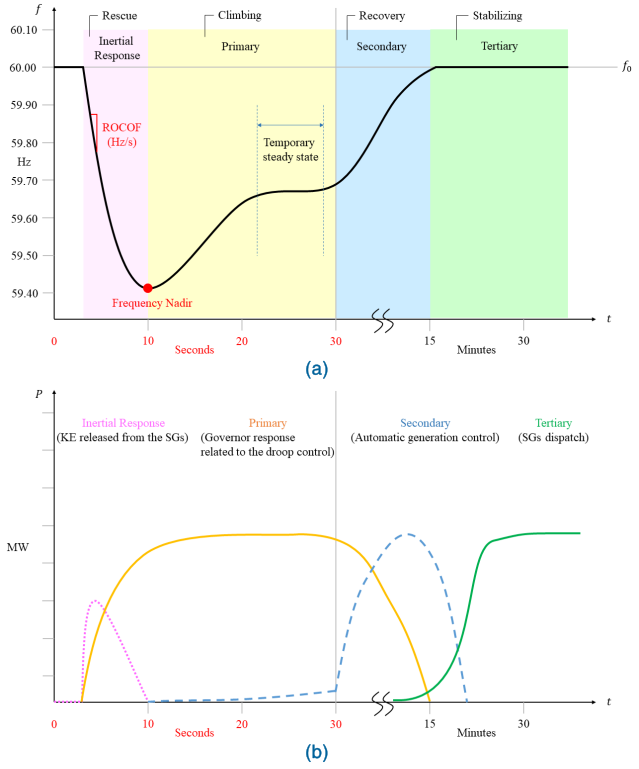

FIGURE 5. The typical phases of the frequency regulation. (a). The frequency response. (b) The corresponding generation responses.

inertial control of the WT can be expressed as:

$$P_{in} = -K_{in} \cdot \frac{df}{dt} \tag{6}$$

where P_{in} is the additional output power of the WT; K_{in} is the gain related to the inertia constant H_D, and f is the measured frequency. Based on (6), it can be observed that the output power of the WT is proportional to the derivative of the frequency. The inertial controller is shown in Fig. 6. A low-pass filter is generally used to filter out noise signals and reduce the overshoot.

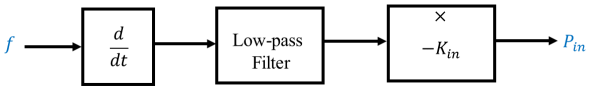

FIGURE 6. Inertial controller.

To imitate the response of the speed governor of a conventional SG, droop control is applied [45]. For droop control, the additional output power P_f is proportional to the frequency deviation of the measured frequency from the nominal frequency, which is expressed as:

$$P_f = \frac{f_0 - f}{R} \tag{7}$$

where f_0 is the nominal frequency and R is the droop constant. The droop controller is shown in Fig. 7. The typical droop characteristics are depicted in Fig. 8.

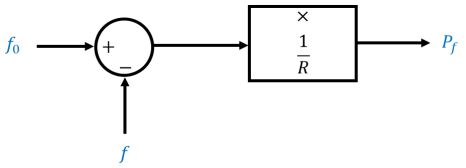

FIGURE 7. Droop controller.

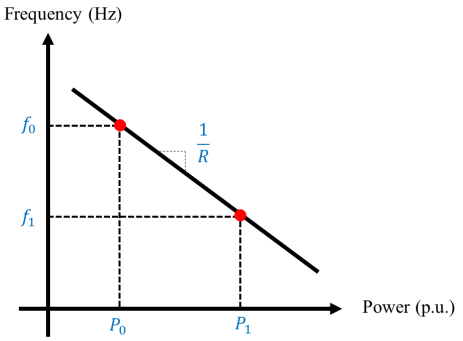

FIGURE 8. Typical droop characteristic of the WT.

As shown in Fig. 8, the slant line with a negative slope represents the frequency versus the output power of a WT. Assuming the original operating point of the WT is (P_0, f_0), when a low-frequency event occurs, the operating point moves toward (P_1, f_1), indicating that the WT should increase its output power to assist the frequency recovery process.

If both inertial control and droop control are applied, then the total additional output power provided by a WT during the frequency event, P_{WT}, can be expressed by combining (6) and (7), as follows:

$$P_{WT} = -K_{in} \cdot \frac{df}{dt} + \frac{f_0 - f}{R} \tag{8}$$

D. BASIC PRINCIPLES OF THE VSC-HVDC SYSTEM

In brief, the VSC-HVDC system can be viewed as a zero-inertia generator that is capable of controlling the active and reactive powers instantaneously [46]. The structure and control of a typical VSC-HVDC-connected WF system are presented in Fig. 9.

The wind-farm side voltage source converter (WFVSC) collects the active power from the WF. It sets the reference frequency, voltage amplitude, and phase angle. Moreover, the power flow between the grid side voltage source converter (GSVSC) and WFVSC can be stabilized by controlling the DC-link voltage. In particular, a constant DC-link voltage indicates a balanced power flow between the grid and WF.

For the purpose of stabilizing the power flow and voltage in the VSC-HVDC system, different control methods at both sides of the converters should be considered. The detailed outer and inner current control loops for the VSC-HVDC system are introduced as follows.

The outer current loop determines the reference currents, which are referred to the synchronous d-q reference frame.

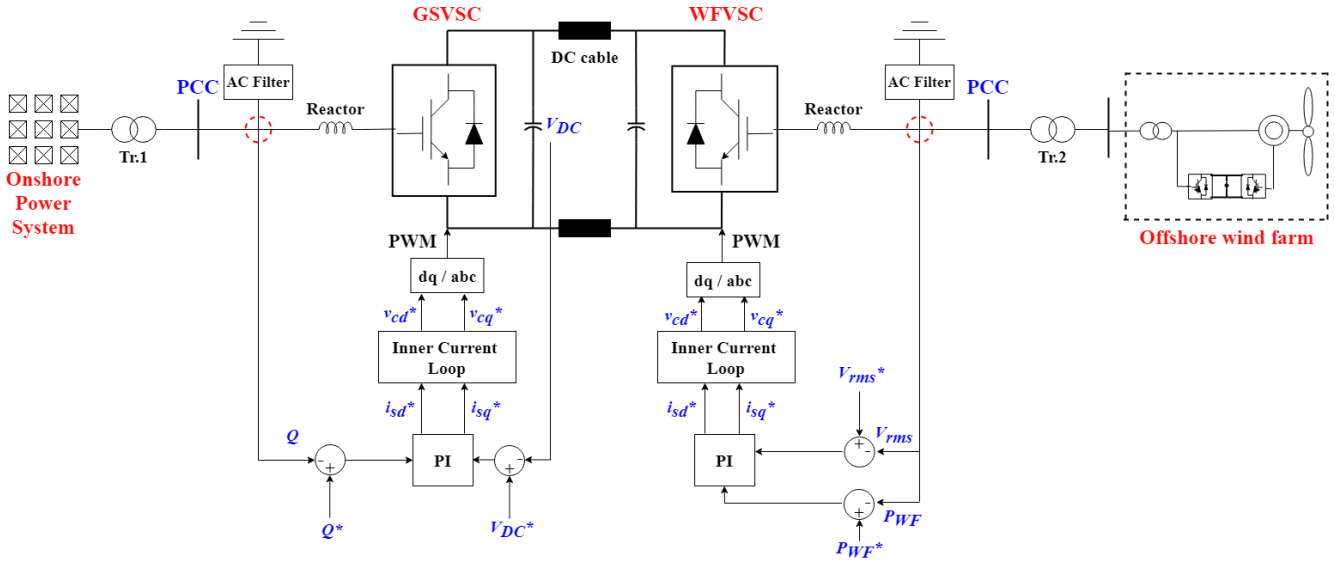

FIGURE 9. The schematic diagram of the VSC-HVDC connected OWF.

The design of the power controllers is based on the power flowing through the converter [2], as shown by:

$$\begin{cases} P = \dfrac{3}{2}\left(v_d i_d + v_q i_q\right) = \dfrac{3}{2} v_d i_d \\ Q = \dfrac{3}{2}\left(v_q i_d - v_d i_q\right) = -\dfrac{3}{2} v_d i_q \end{cases} \tag{9}$$

where v_d and v_q are the d-axis and q-axis voltages, respectively, and i_d and i_q are the d-axis and q-axis currents, respectively.

To enable the WFVSC to control the captured active power from the WF, the active power controller can be designed according to (9). It is shown in Fig. 10, where P_{WF}^* is the reference active power from the WF and i_d^* is the reference d-axis current.

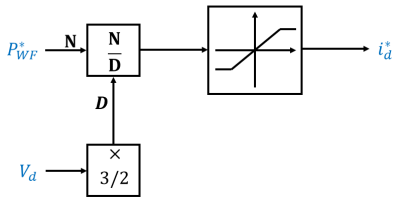

FIGURE 10. Active power controller based on the power equations.

Generally, the reference values of the d-axis and q-axis currents can be determined by two types of inputs, which depend on the system operators. The common outer current loop is shown in Fig. 11, where V_{DC} is the DC-link voltage, v_{rms} is the AC voltage at the point of common coupling (PCC), and i_q^* is the reference value of the q-axis current.

To derive the inner current loop, the electrical circuit of the VSC-HVDC is analyzed. The equivalent circuit of the VSC-HVDC is shown in Fig. 12, where the left part of the

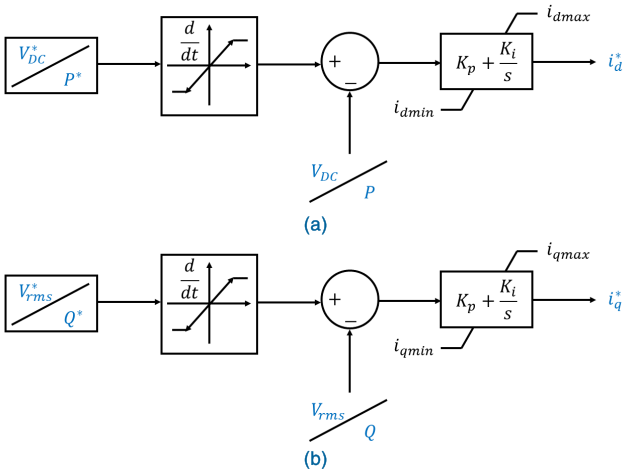

FIGURE 11. (a) DC voltage controller and active power controller. (b) AC voltage controller and reactive power controller.

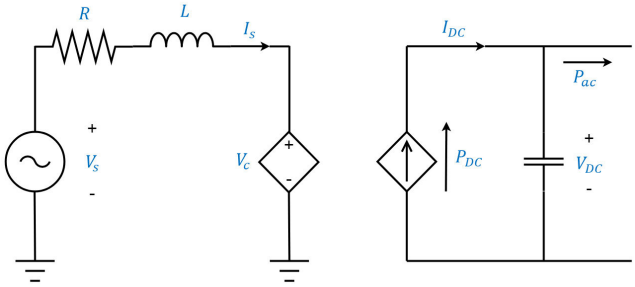

FIGURE 12. The equivalent circuit of the VSC-HVDC system.

diagram is the AC side and the right part is the DC side. L and R represent the equivalent inductance and resistance of the reactor and the transformer, respectively. V_s is the AC side

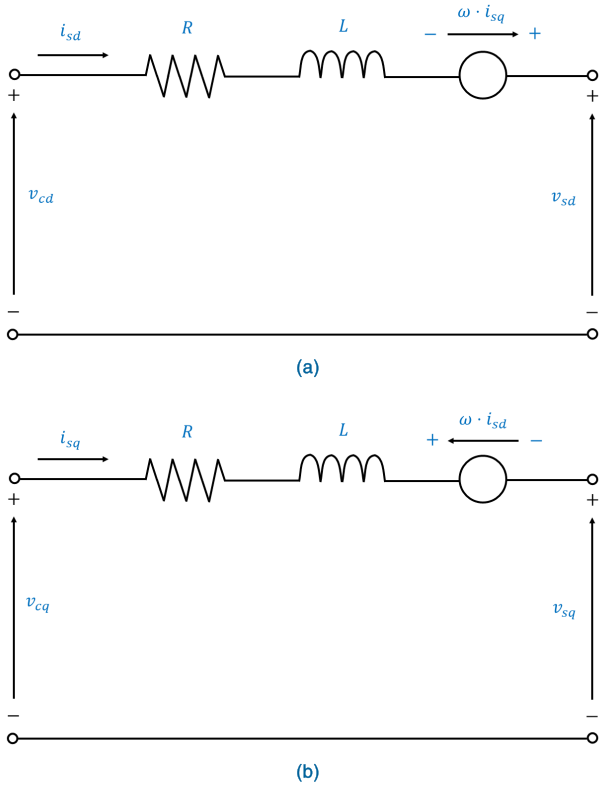

FIGURE 13. (a) The d-axis equivalent circuit model and (b) the q-axis equivalent circuit model of the VSC-HVDC system.

voltage and V_C is the output voltage of the converter [47]. Coupling between the AC and the DC sides is achieved through a controlled voltage source and a controlled current source.

Subsequently, the abc voltage vectors are transformed to dq0 voltage vectors through Park's transformation to control the VSC-HVDC. The d-axis and q-axis equivalent circuit models are depicted in Fig. 13. The dynamic equations describing the equivalent circuits are expressed as:

$$\begin{aligned} v_{cd} &= Ri_{sd} + L\frac{di_{sd}}{dt} + v_{sd} - i_{sq}\omega L \\ v_{cq} &= Ri_{sq} + L\frac{di_{sq}}{dt} + v_{sq} + i_{sd}\omega L \end{aligned} \tag{10}$$

where v_{cd} and v_{cq} are the d-axis and q-axis output voltages of the converter, respectively; v_{sd} and v_{sq} are the d-axis and q-axis grid AC-side voltages, respectively, and ω is the synchronous angular velocity. The grid AC voltage can be further derived from (10):

$$\begin{aligned} v_{sd}^* &= Ri_{sd} + L\frac{di_{sd}}{dt} = \left(K_p + \frac{K_i}{s}\right)\left(i_{sd}^* - i_{sd}\right) \\ v_{sq}^* &= Ri_{sq} + L\frac{di_{sq}}{dt} = \left(K_p + \frac{K_i}{s}\right)\left(i_{sq}^* - i_{sq}\right) \end{aligned} \tag{11}$$

where v_{sd}^* and v_{sq}^* are the reference values of the d-axis and q-axis grid AC voltages, respectively, and i_{sd}^* and i_{sq}^* are generated from the outer current loop. Accordingly, by substituting (11) into (10), the inner current loop is derived as:

$$\begin{aligned} v_{cd}^* &= \left(K_p + \frac{K_i}{s}\right)\left(i_{sd}^* - i_{sd}\right) + v_{sd} - i_{sq}\omega L \\ v_{cq}^* &= \left(K_p + \frac{K_i}{s}\right)\left(i_{sq}^* - i_{sq}\right) + v_{sq} + i_{sd}\omega L \end{aligned} \tag{12}$$

The control diagram of the inner current loop is shown in Fig. 14. The d-axis and q-axis components are decoupled to control the active and reactive powers or the DC and AC voltages separately. Next, the reference values of the output voltages of the converter, i.e., v_{cd}^* and v_{cq}^*, are transformed into abc voltage vectors through an inverse Park's transformation to generate the reference signals for pulse width modulation (PWM), which produces the signals for controlling the switches.

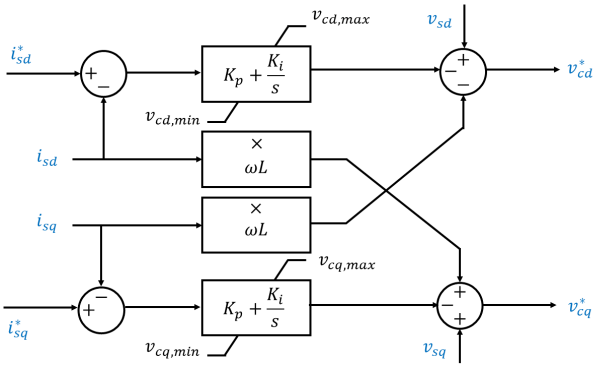

FIGURE 14. The inner current loop of the VSC-HVDC.

A constant DC-link voltage ensures the power balance between the GSVSC and WFVSC. By contrast, the power flow can be regulated by adjusting the DC-link voltage, V_{DC}. Obviously, since the capacitors in the DC-link are the storage elements, they can be used to release the stored energy or absorb the excess energy by reducing or increasing V_{DC}, respectively. The energy change W_C via the equivalent capacitance C and the power change P_C in the period of $t_1 - t_2$ are expressed as:

$$W_c = C\int_{V_{DC}(t_1)}^{V_{DC}(t_2)} V_{DC}\cdot dV_{DC} \tag{13}$$

$$P_c = \frac{dW_c\left(t_1, t_2\right)}{dt} \tag{14}$$

Consequently, when the system frequency falls, the DC capacitors can release the stored energy to the grid. By contrast, when the system frequency increases, the DC capacitors can absorb the extra energy. By regulating the DC voltage, the VSC-HVDC will be able to contribute to FR.

III. FREQUENCY REGULATION STRATEGIES FOR A VSC-HVDC-CONNECTED WF

In fact, the VSC-HVDC and the WTs cannot provide frequency support if there is no additional controller. In order to let the VSC-HVDC and the WTs participate in FR,

the synthetic inertia techniques turn out to be an essential component. In recent years, several FR strategies for VSC-HVDC-connected OWFs have been proposed. This study summarizes the main strategies and makes a detailed comparison of them. The classification of these FR strategies is presented in Fig. 15. Two aspects are considered for the classification: 1) whether the grid frequency is communicated to the WF side and 2) the algorithm for the WF to perceive the grid frequency disturbance. A detailed introduction to these strategies is presented in the following sections.

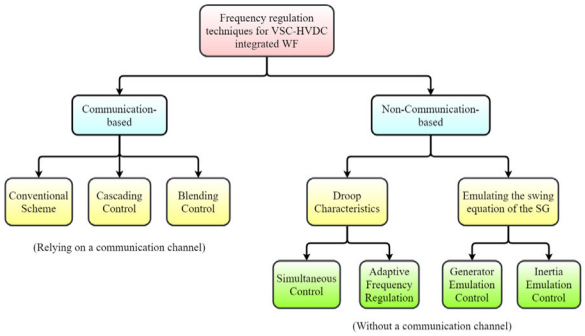

FIGURE 15. The classification of the frequency regulation techniques for VSC-HVDC integrated WF.

A. CONVENTIONAL SCHEME (COMMUNICATION-BASED APPROACH)

The idea of the conventional scheme is to use a communication link to transmit the grid frequency signal to the WF [48]. This type of method can be categorized as a communication-based approach. In general, the conventional scheme relies on a supervisory control and data acquisition system or other fast communication links. To enable a VSC-HVDC-connected WF to provide frequency support, the WFVSC should be operated under an AC voltage and active power control, while the GSVSC should keep the DC-link voltage constant. A schematic diagram of the conventional scheme is depicted in Fig. 16. With a reliable and accurate communication channel, the conventional scheme allows WFs to participate in FR. However, the communication of the grid frequency may result in the delay of frequency support from the WF. Hence, the transmission time delay should be reduced as much as possible.

B. SIMULTANEOUS CONTROL

When using the communication-based method, there is a concern regarding the reaction time and the reliability of the dynamics of the WF. For example, the ROCOF and the frequency nadir can be more significant if there is a delay in the WF providing frequency support. Since information transmission involves measurement, processing, communication, and reception, the typical delay values are in the range of 50 ms – 1 s [49] [50]. Some researchers proposed an alternative based on DC-link voltage regulation to address the problem of transmission delay [48], [51]–[53].

The principle of simultaneous control is that a system frequency disturbance first changes the DC-link voltage of the VSC-HVDC in case of power imbalance in the main grid. When the DC voltage is changed, the DC capacitors immediately release or absorb the energy. Next, the deviation of DC voltage contributes to a new WFVSC frequency. Thus, the WF will provide frequency support according to the new WFVSC frequency.

The control scheme for simultaneous control is shown in Fig. 17, where V_{DC}^* is the reference value of the DC voltage; V_{DC0} is the initial DC voltage; f is the nominal grid frequency; f_{WF}^* is the reference value of the WFVSC frequency and f_{WF0} is the nominal WFVSC frequency. The equations that describe the simultaneous control are expressed as:

$$\Delta V_{DC} = V_{DC}^* - V_{DC0} = K_A \cdot \Delta f \tag{15}$$

$$\Delta f_{WF} = f_{WF}^* - f_{WF0} = K_B \cdot \Delta V_{DC} \tag{16}$$

$$\Delta f_{WF} = K_A K_B \Delta f \tag{17}$$

where Δf_{WF} is the deviation of the WFVSC frequency from the nominal value and K_A and K_B are the multipliers. The larger the values of K_A and K_B, the larger the deviations of the DC voltage and the WFVSC frequency will be. Thus, the DC capacitors and the WTs will be able to provide more active power to the grid. The WFVSC frequency and the grid frequency are strongly correlated through (17). If the product of K_A and K_B is equal to one, then the WFVSC frequency will exhibit a similar dynamic response as the grid frequency.

Notably, simultaneous control does not need an additional communication channel to transmit the grid frequency to the WFVSC. In addition, reference [54] analyzed the effects of different time delays and controller parameters for the conventional scheme and simultaneous control and showed that simultaneous control yields more stable dynamics in P, V_{DC} and f during the FR period.

C. INERTIA EMULATION CONTROL FOR A VSC-HVDC SYSTEM

Although the VSC-HVDC and WF can participate in FR by using the two former strategies, the performance is questionable because of the communication latency or the V_{DC} variation process. That is, the derivation of (15), (16), and (17) should be closely analyzed. If the VSC-HVDC can provide frequency support, then its inertia constant should be found. To verify the synthetic inertia of the VSC-HVDC and WF, several researchers have addressed the issue of inertia emulation control (IEC) strategies for the VSC-HVDC [55]–[58]. The concept of IEC is to let the non-synchronous units emulate the behaviors of SG. The authors of [55] proposed a coordinated control strategy for a WF with line-commutated-converter-based HVDC for providing frequency support. The method introduces a virtual droop constant for the HVDC and thus enhances the overall FR performance. It is noted that the WF does not require the additional frequency controller, and the electrical power of the WF is determined by the delivered power of the HVDC. Hence, the mechanical power and the

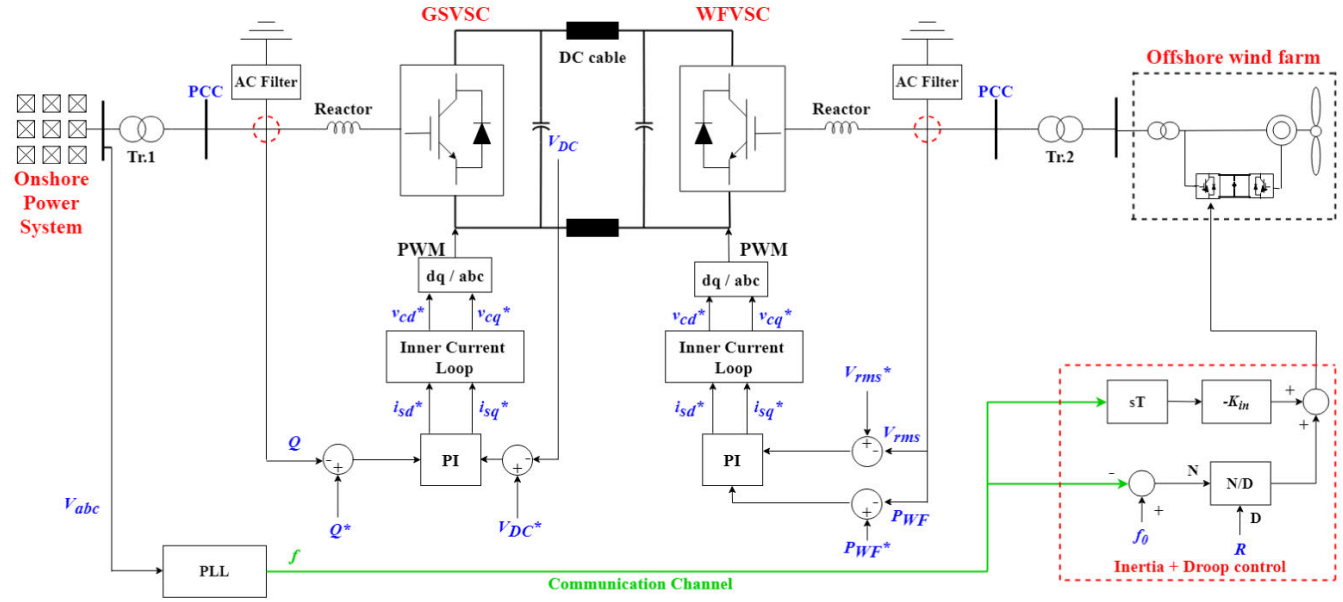

FIGURE 16. The schematic diagram of the conventional scheme.

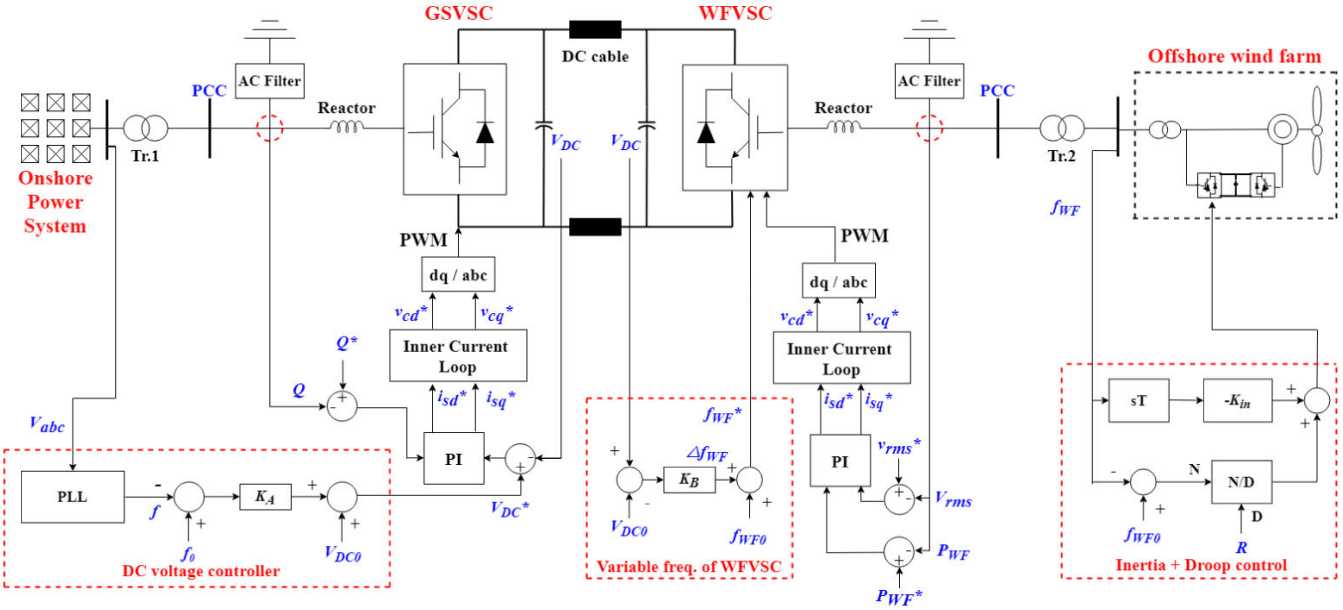

FIGURE 17. The schematic diagram of the simultaneous control.

pitch angle can be changed to match the electrical power. Reference [56] demonstrates a coordinated control strategy by using the DC capacitor energy and the KE of the WF to improve the overall system inertia. The strategy can provide more inertia support than the single VSC-HVDC or single WF control by assuming the virtual inertial time constants for the VSC-HVDC and WF.

In general, the step-by-step IEC algorithm for the VSC-HVDC is as follows:

1) Capacitor DC voltage versus system frequency.
2) Emulated inertia constant versus SG inertia constant.
3) Design of the DC-link voltage controller.
4) WF side frequency deviation versus DC voltage deviation.

The inertia constant H of an SG can be expressed as

$$H = \frac{E_K}{S} = \frac{\frac{1}{2}J\omega_0^2}{S} \tag{18}$$

where E_K is the stored kinetic energy at synchronous speed ω_0 and S is the machine rating in MVA [59].

For steps 1) and 2), by mapping the KE of the SG into the electromagnetic energy of the DC-link capacitors, the emulated inertia constant of VSC-HVDC H_{VSC} can

be obtained as:

$$H_{VSC} = \frac{E_e}{S_{VSC}} = \frac{\frac{1}{2}NCV_{DC0}^2}{S_{VSC}} \tag{19}$$

where E_e is the electromagnetic energy of the DC-link capacitors, N is the total number of capacitors installed in the DC-link, C is the capacitance of the DC-link and S_{VSC} is the capacity of the VSC converter. The electromagnetic energy stored in the DC-link capacitors is very similar to the KE of the SG because the angular speed of the SG and the nominal DC voltage are squared.

The swing equation describing the rotor motion of the SG can be expressed as:

$$\frac{2HS}{(f_0)^2} \cdot f \cdot \frac{df}{dt} = P_m - P_e[MW] \tag{20}$$

where P_m is the mechanical power inputted to the machine and P_e is the electrical power. Equation (20) can be simplified by approximating $f \approx f_0$ and using the per-unit expression as:

$$\frac{2H}{f_0} \cdot \frac{df}{dt} = P_m - P_e[pu] \tag{21}$$

The target is to equate the exchange power of VSC-HVDC to that of an SG. Hence, equation (21) can be modified by substituting H_{VSC} for H, V_{DC} for f and V_{DC0} for f_0, as follows:

$$\frac{NCV_{DC}}{S_{VSC}} \cdot \frac{dV_{DC}}{dt} = P_{in} - P_{out}[pu] \tag{22}$$

Equation (22) reveals that the variation of V_{DC} also changes the active power through the VSC-HVDC, as well as the stored energy in the DC-link capacitors.

Next, to investigate the relationship between C, S_{VSC}, H_{VSC}, V_{DC} and f, equating (21) and (22) yields

$$\frac{2H_{VSC}}{f_0} \cdot \frac{df}{dt} = \frac{NCV_{DC}}{S_{VSC}} \cdot \frac{dV_{DC}}{dt} \tag{23}$$

By integrating the left side of (23) from f_0 to f and the right side of (23) from V_{DC0} to V_{DC}, the corresponding integration and its solution can be expressed as, respectively:

$$\int_{f_0}^{f} \frac{2H_{VSC}}{f_0} \cdot df = \int_{V_{DC0}}^{V_{DC}} \frac{NCV_{DC}}{S_{VSC}} \cdot dV_{DC} \tag{24}$$

$$\frac{2H_{VSC}}{f_0} \cdot (f - f_0) = \frac{NC}{2S_{VSC}} \left(V_{DC}^2 - V_{DC0}^2\right) \tag{25}$$

Rearranging (25) and letting $\Delta f = f - f_0$, $\Delta V_{DC} = V_{DC} - V_{DC0}$ result in:

$$H_{VSC} \cdot 2 \cdot \frac{\Delta f}{f_0} = \frac{NC \cdot V_{DC0}^2}{2S_{VSC}} \left[\left(\frac{\Delta V_{DC}}{V_{DC0}} + 1\right)^2 - 1\right] \tag{26}$$

$$H_{VSC} = \frac{\frac{1}{2} \cdot \frac{NC \cdot V_{DC0}^2}{S_{VSC}} \left[\left(\frac{\Delta V_{DC}}{V_{DC0}} + 1\right)^2 - 1\right]}{2 \cdot \frac{\Delta f}{f_0}} \tag{27}$$

Equation (27) reveals that the change of DC-link voltage ΔV_{DC} is strongly related to the frequency deviation Δf for a given emulated time constant H_{VSC}. Because H_{VSC} is always positive, the sign of ΔV_{DC} is the same as that of Δf, e.g., $\Delta f < 0$ implies $\Delta V_{DC} < 0$ and vice versa. To evaluate the effect of ΔV_{DC} and Δf on the emulated time constant H_{VSC}, their trends containing different H_{VSC} values for variable f and V_{DC} are drawn in Fig. 18. It can be seen from Fig. 18 that a larger H_{VSC} leads to a larger ΔV_{DC} for a given Δf as a larger H_{VSC} means a larger energy exchanged with the grid when the grid frequency changed. Furthermore, the effect of different values of C with fixed H_{VSC} is investigated in Fig. 19. It is shown that the DC-link voltage changes within a smaller range with a larger capacitance compared to the case with a smaller capacitance. In conclusion, it is a trade-off between a larger H_{VSC} and the cost of larger C for ΔV_{DC} within the acceptable range of $\pm 10\%$.

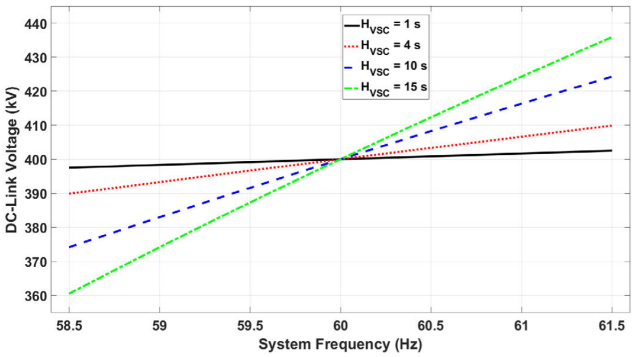

FIGURE 18. The relation between f, V_{DC} for different values H_{VSC} with total capacitance 2 × 7.5 mF.

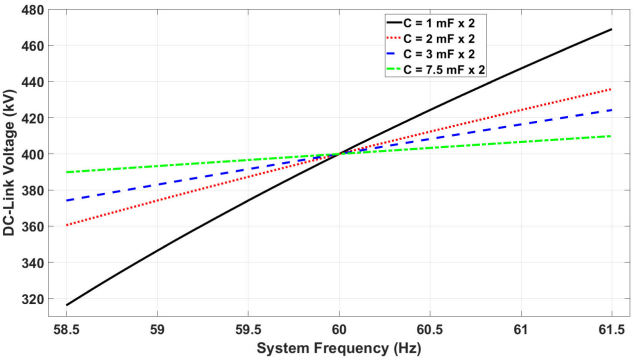

FIGURE 19. The relation between f, V_{DC} for different values of total capacitance with H_{VSC} = 4 s.

Recalling step 3), the DC-link voltage controller is required to deploy the emulated inertia of the VSC-HVDC. Equation (25) can be modified as (28) by letting $V_{DC}^* = V_{DC}$.

$$V_{DC}^* = \sqrt{\frac{4S_{VSC}H_{VSC}}{NCf_0} \cdot f - \frac{4S_{VSC}H_{VSC}}{NC} + V_{DC0}^2} \tag{28}$$

As a result, the reference DC-link voltage V_{DC}^* can be determined by the grid frequency f. The corresponding schematic diagram of the IEC with the DC-link voltage controller is shown in Fig. 20. In addition, the WF can participate in FR by using (16) to perceive the grid frequency

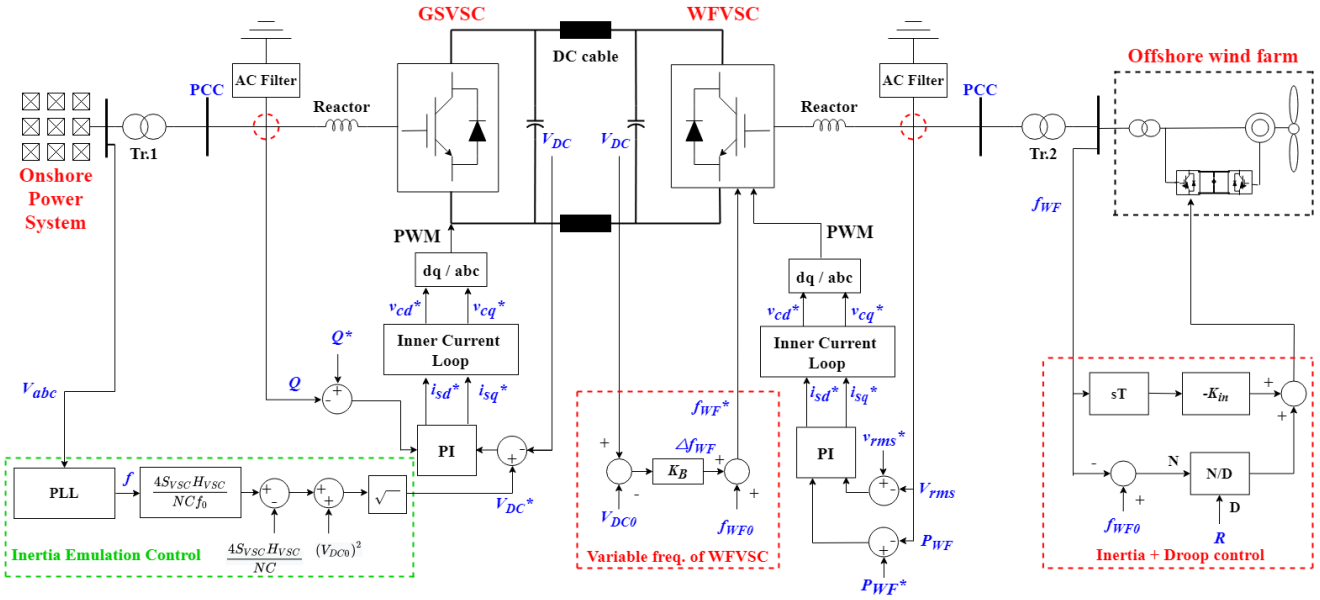

FIGURE 20. The schematic diagram of the IEC for VSC-HVDC connected WF.

disturbance. In this way, step 4) is completed via the artificial coupling between the grid frequency and the WF frequency.

D. BLENDING CONTROL OF VSC-HVDC AND WF FOR FAST FREQUENCY RESPONSE

To enhance the inertial response and improve the overall FR capability, the authors of [57] and [60] proposed to utilize the energy stored in the DC-link capacitors during the DC voltage variation. However, using the stored energy in the DC-link capacitors to provide a fast inertial response has the serious disadvantage of requiring an extremely large capacitance. Rather than solely relying on the frequency support from the VSC-HVDC or WF, blending the energy stored in the VSC-HVDC and the kinetic energy of the WTs to provide frequency support can yield better performance.

The author of [60] proposed another IEC strategy that can provide a fast frequency response while not requiring a very large capacitance nor excessive active power from the WF. That is, the high-performance WT is not required. The inertia emulation control is developed for the VSC-HVDC. The more detailed process of derivation can be found in [60]; this paper merely shows the key concepts. The step-by-step derivation of the controller is described as follows.

The aim is to obtain an inertia constant for the VSC-HVDC. That is, the VSC-HVDC can provide inertial response when the grid frequency changes. Therefore, the relationship between the active power flowing through the GSVSC and the grid frequency can be expressed in a swing equation as:

$$\frac{2H_{VSC}S_{VSC}}{(f_0)^2}f\frac{df}{dt} = P_{in} - P_{out}[W] \tag{29}$$

where H is the emulated inertia constant of the converter, S is the rated capacity of the VSC converter, P_{in} is the input active power of the GSVSC, and P_{out} is the output active power toward the grid.

Assuming the grid frequency drops, the reference active power resulting from inertia response P_H^* can be found from

$$\begin{aligned} P_H^* &= P_{out} - P_{in} = -\frac{2H_{VSC}S_{VSC}}{(f_0)^2}f\frac{df}{dt} \\ &\approx -\frac{2H_{VSC}S_{VSC}}{f_0}\frac{df}{dt} \end{aligned} \tag{30}$$

For example, if the emulated inertia constant of the VSC-HVDC is 4 s, which is the same as the typical value of a conventional SG [61], [62], and the rated capacity of the converter is 300 MVA in a 60 Hz system, then the active power P_H^* is 20 MW when the ROCOF is −0.5 Hz/s.

The reference value of the variation of DC-link voltage can be obtained from the reference active power [60]

$$\Delta V_{DC}^* = -\frac{1}{CV_{DC0}}\frac{\tau}{\tau s + 1}P_H^*\,(s) \tag{31}$$

where τ is a designed parameter as well as a time constant relating to the variation of DC-link voltage and the dynamic of the WF and it is defined as a third of the reference settling time of the WF. Considering that the WF needs 0.3 s to adjust its output power to the reference value, for example, i.e., $3\tau = 0.3$ s, the resulting time constant τ can be obtained as 0.1 s.

The reference active power of the WF is determined by a simple DC voltage-active power droop controller

$$P_{WF}^* = \frac{CV_{DC0}}{\tau}(V_{DC0} - V_{DC}) = K_{WF}(V_{DC0} - V_{DC}) \tag{32}$$

where K_{WF} is the gain affecting the amount of output power of the WF. Overall, the active power flowing through the

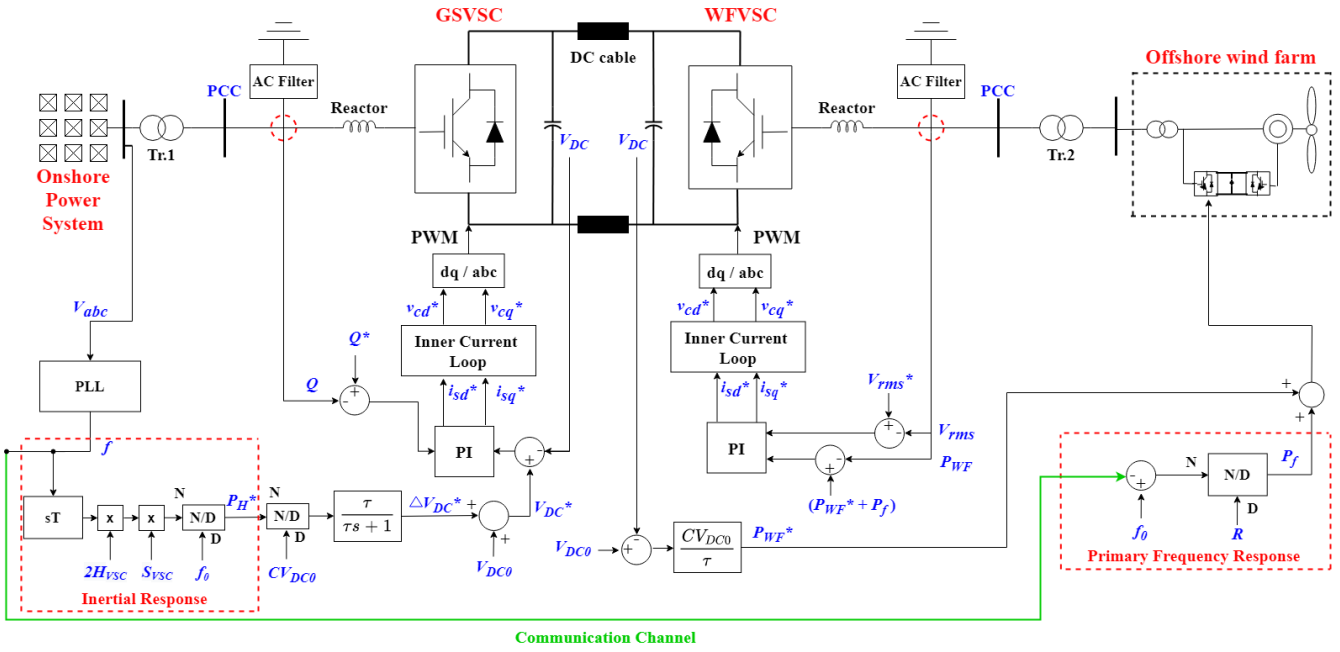

FIGURE 21. The schematic diagram of the blending control of the VSC-HVDC and the WF for fast frequency response.

GSVSC can be expressed as

$$P(s) \approx \underbrace{\frac{\pi s}{\pi s+1} P_H^*(S)}_{\text{from VSC-HVDC}} + \underbrace{\frac{1}{\pi s+1} P_H^*(S)}_{\text{from WF}} = P_H^*(s) \qquad (33)$$

where the former term denotes the active power from the VSC-HVDC and the latter term denotes the contribution from the WF. By introducing (33) into the control scheme and deploying a larger value of τ, the WF is not required to ramp up its output power as quickly as the method introduced in Section III B. However, the larger τ also leads to a larger deviation of the DC-link voltage. It is a trade-off between the requirement of a high-performance WF and the large deviation of the DC-link voltage. By combining (30) – (33), the corresponding control diagram for this inertia emulation control is shown in Fig. 21.

E. MODIFIED VSC CONTROL WITH ANCILLARY FREQUENCY CONTROL

In [46], the GSVSC and WFVSC are equipped with the ancillary frequency controller to adjust the modulation indices for PWM. To detect the frequency disturbance at the grid side, the reference frequency at the WFVSC, f_{WF}^*, is made time-varying according to the grid frequency f, by applying an ancillary frequency controller. This is shown in Fig. 22 (a), where V_{WF} is the AC voltage at the PCC of the WFVSC; m_a is the amplitude modulation index for PWM and f_{WF} is the frequency at the WFVSC. The grid frequency f is transmitted to the WFVSC through a transmission channel. As a consequence, the OWF can provide frequency support by detecting the frequency at the WFVSC.

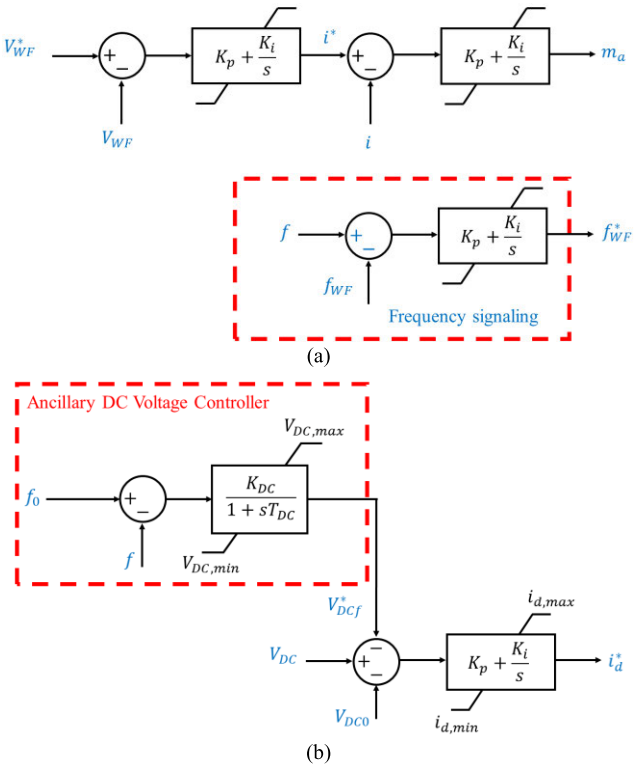

FIGURE 22. (a) The ancillary frequency controller for WFVSC. (b) The ancillary DC voltage controller for GSVSC.

As for the GSVSC, an ancillary DC voltage controller can be added to regulate the DC-link voltage according to the grid frequency, as shown in Fig. 22 (b), where V_{DCf}^* is

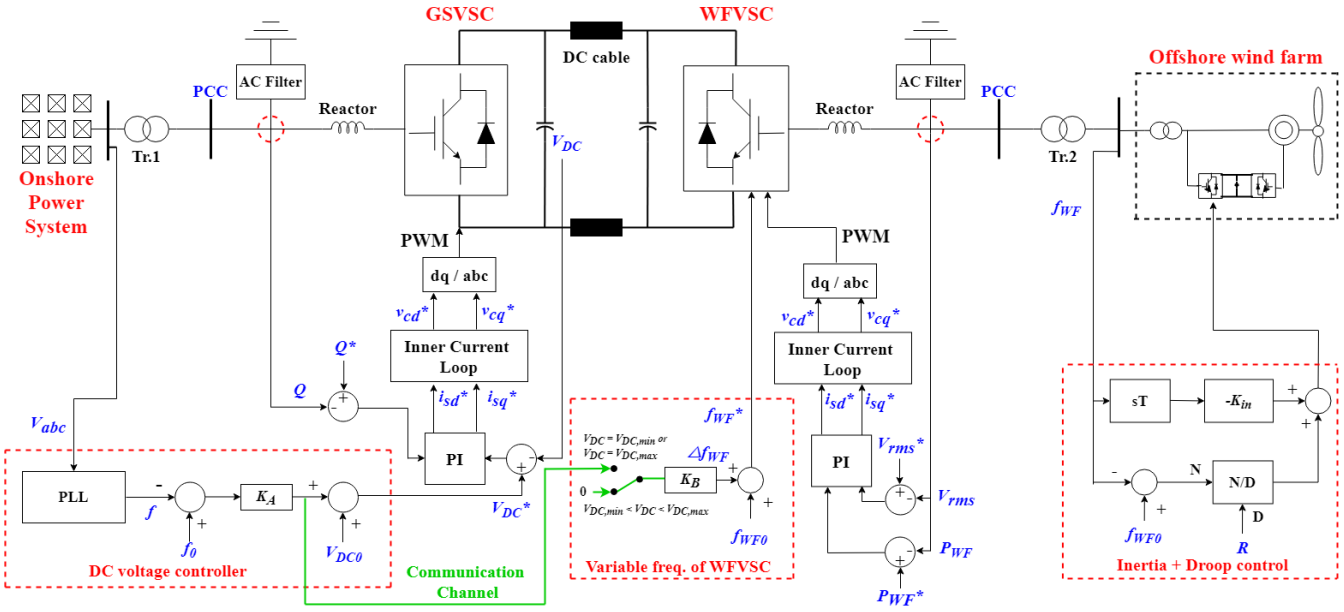

FIGURE 23. The schematic diagram of the cascading control.

the additional reference value of DC voltage based on the deviation between the measured frequency f and the nominal frequency f_0. The amount of V_{DCf}^* is decided by the gain, K_{DC}. The time constant T_{DC} of the first-order transfer function represents the speed of the variation of stored energy of the DC capacitors. The upper limit, $V_{DC,max}$, is set to +0.1 p.u., while the lower limit, $V_{DC,min}$, is set to -0.1 p.u. to ensure the safe operation of DC voltage. Thus, the DC capacitors can be utilized to release or absorb the energy based on the frequency deviation.

However, one of the disadvantages of the above strategy is the latency issue due to the frequency signaling. Thus, the WTs need to monitor the WFVSC frequency, which is affected by the frequency signal transmitted through a communication interface from the grid. Nevertheless, this process seems to be superfluous because the grid frequency can be directly transmitted to the OWF rather than the WFVSC. In addition, the variation of the WFVSC frequency is regulated by a PI controller, which increases the operation time and slows down the response of the WTs.

F. CASCADING CONTROL

Although all the methods in Section III A - E can achieve the function of FR, they ignore the dynamics of the generator rotor speed of the WTs. In particular, the variation of rotor speed can affect the operation of WTs and the wind energy harvesting, and even can cause a worse frequency disturbance, i.e., the SFD. Consequently, the authors of [63] proposed a method called cascading control that can ensure a small variation of rotor speed for WTs and a high wind energy harvest. The difference between simultaneous control and cascading control is that the latter sets a higher priority for the VSC-HVDC than the OWF for providing frequency support. That is, the OWF can provide inertia support only when the DC voltage of the VSC-HVDC reaches the limit. Therefore, the OWF is the last resort for providing inertia support. In the cascading control, a communication channel is established to transmit the grid frequency to the WFVSC. Furthermore, the WTs can also provide frequency support according to the grid frequency.

The overall control scheme for cascading control is shown in Fig. 23. To achieve sequential utilization of the stored energy in the VSC-HVDC and the inertia support from the OWF, an appropriate deadband for the deviation of WFVSC frequency from the nominal value Δf_{WF} is designed as:

$$\Delta f_{WF} = \begin{cases} K_A K_{DC} \Delta f & \text{when} V_{DC} = V_{DC,min} \text{or} V_{DC} = V_{DC,max} \\ 0 & \text{when} V_{DC,min} < V_{DC} < V_{DC,max} \end{cases} \tag{34}$$

From (34), the WFVSC frequency does not change when the DC voltage is within the normal range, and the WT operates in its MPPT mode. Thus, the wind energy harvesting and economic profit are guaranteed.

G. GENERATOR EMULATION CONTROL FOR VSC-HVDC-CONNECTED OWF

Using the fast communication channel to transmit the grid frequency signal to the WF may have a high cost. Moreover, if the VSC-HVDC is designed to provide a large inertia support, then the DC-link capacitors will have large volumes and high cost. Thus, another method called generator emulation control (GEC) was proposed to fix these problems. The GEC was first applied to the PV inverter to provide

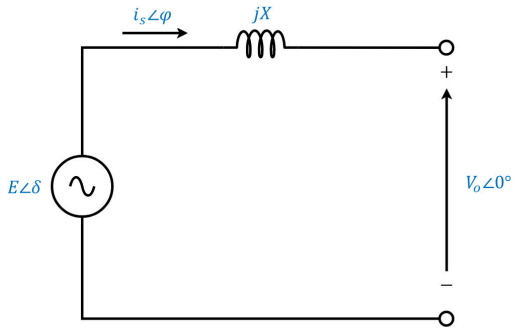

FIGURE 24. The equivalent circuit model of the SG ignoring the internal resistance.

synthetic inertia [64]. Consequently, this technique can also be applied to VSC-HVDC [65]. By using GEC, the VSC-HVDC can emulate the behavior of a conventional SG to provide synthetic inertia.

Under a three-phase balance and ignoring the loss caused by the internal resistance of the SG, the equivalent model of an SG is constructed and is shown in Fig. 24, where E is the internal EMF of the SG; X is the equivalent reactance; i_s is the current flowing out of the SG; V_o is the terminal voltage of the SG and δ is the difference in phase angle between E and V_o. If V_o is constant and δ is marginal, then the output active power of the SG can be expressed as:

$$P_o = \frac{|V_o|\,|E|}{X} sin\,\delta \approx \frac{|V_o|\,|E|\,\delta}{X} \tag{35}$$

After the SG is connected to the power system, the grid frequency disturbance will affect the power output from the SG. Thus, Equation (35) is rewritten as:

$$\begin{aligned} P_o &= \frac{|V_o|\,|E|}{X} \int \left(\omega_{gen} - \omega_{grid}\right) dt \\ &= k_s \int \left(\omega_{gen} - \omega_{grid}\right) dt \end{aligned} \tag{36}$$

where k_s is equal to $|V_o|\,|E|\,/X$, ω_{gen} is the electrical angular frequency of the EMF, and ω_{grid} is the electrical angular frequency of the grid voltage.

If the rotor dynamics of the SG are considered, then the inertial behaviors of the SG can be expressed in a swing equation. Therefore, ω_{gen} is expressed as:

$$\omega_{gen} = k_g \int \left(P_i - P_o\right) dt \tag{37}$$

where k_g is the gain related to the number of poles and the moment of inertia. The speed governor of the SG possesses the frequency–active power droop characteristic for primary frequency support. Thus, the additional input power P_i owing to the droop characteristics is expressed as:

$$P_i = k_d \left(\omega_{ref} - \omega_{gen}\right) \tag{38}$$

where k_d is the gain related to the droop constant and ω_{ref} is the reference value of rotor speed, i.e., nominal speed. By combining (36), (37) and (38), the dynamic model of the SG with the frequency–active power droop control is found and is shown in Fig. 25.

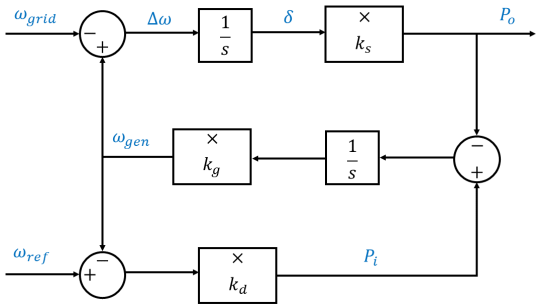

FIGURE 25. Dynamic model of the SG equipped with the frequency – active power droop characteristic.

Given the dynamic model (Fig. 25), the transfer function is derived from the signal flow graph and Mason's gain formula [66]. Fig. 26 depicts the signal flow graph based on Fig. 25. Based on the signal flow graph, the step-by-step derivation of the transfer function is presented as follows.

$$\Delta = 1 - \left[-\frac{k_s K_g}{s^2} - \frac{k_g k_d}{s}\right] = 1 + \frac{k_s k_g}{s^2} + \frac{k_g k_d}{s} \tag{39}$$

$$M_1 = -\frac{k_s}{s}, \quad \Delta_1 = 1 + \frac{k_g k_d}{s} \tag{40}$$

$$\frac{P_o\,(s)}{\omega_{grid}\,(s)} = \frac{M_1 \Delta_1}{\Delta} = \frac{-k_s\left(s + k_g k_d\right)}{s^2 + k_g k_d s + k_s k_g} \tag{41}$$

where Δ is the determinant of the graph; M_1 is the gain of the forward path from ω_{grid} to P_o, and Δ_1 is the part of Δ that is nontouching with the forward path from ω_{grid} to P_o. As a consequence, the transfer function between the output power and the grid frequency in a short-term or high frequency range, can be expressed as Equation (42). By contrast, the transient response in a long-term or low frequency range is expressed as Equation (42).

$$\begin{aligned} lim_{s\to\infty} \frac{P_o\,(s)}{\omega_{grid}\,(s)} &= \frac{-k_s\left(s + k_g k_d\right)}{s\left(s + k_g k_d\right) + k_s k_g} \approx \frac{-k_s\left(s + k_g k_d\right)}{s\left(s + k_g k_d\right)} \\ &= -\frac{k_s}{s} \end{aligned} \tag{42}$$

$$lim_{s\to\infty} \frac{P_o\,(s)}{\omega_{grid}\,(s)} = \frac{-k_s\left(k_g k_d\right)}{k_s k_g} \approx -\frac{k_g k_d}{k_g} \approx -k_d \tag{43}$$

Equations (42) and (42) represent the inertial response and the droop characteristic of an SG, respectively. According

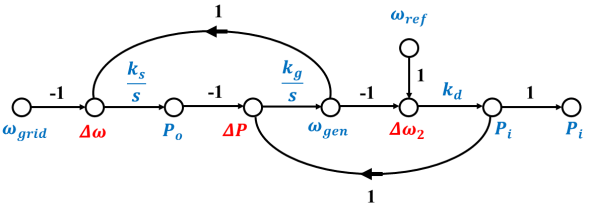

FIGURE 26. The signal flow graph of the block diagram of Fig. 25.

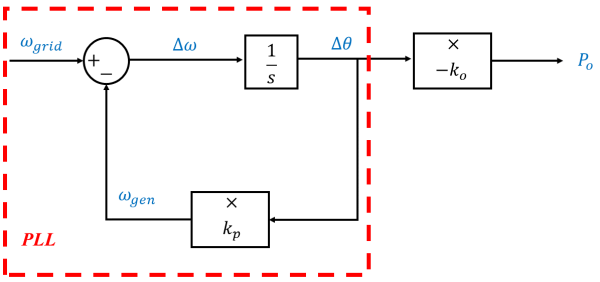

FIGURE 27. The simplified phase locked loop based on Fig. 25.

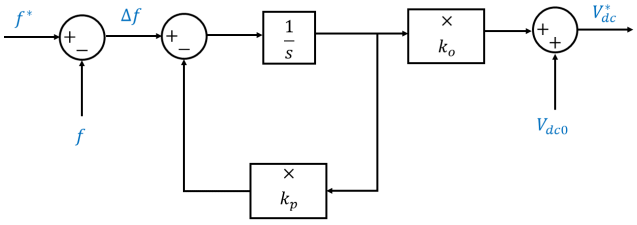

FIGURE 28. The modified GEC controller for adjusting the DC-link voltage.

to [64], Fig. 25 is transformed into a simplified PLL, as shown in Fig. 27. The transfer function of the PLL is expressed as:

$$\frac{P_o(s)}{\omega_{grid}(s)} = -\frac{k_o}{s+k_p} \tag{44}$$

where k_o is the output gain of the GEC controller. Equation (44) can be approximated as $-k_o/s$ in a high frequency range, which is the same as (42). Equation (44) can be approximated as $-k_o/k_p$ in a low frequency range, which is similar to the droop characteristic in (42). Consequently, the PLL can be used to represent the dynamics of the SG.

The PLL enables the VSC-HVDC to emulate the behavior of the SG. To adjust the value of DC voltage of the VSC-HVDC when a frequency disturbance occurs, the modified GEC controller was proposed and shown in Fig. 28 [65]. The corresponding equation of the controller for adjusting the DC-link voltage is:

$$V_{DC}^* = V_{DC0} + \frac{k_o}{s+k_p}\left(f - f^*\right) \tag{45}$$

Hence, the DC-link voltage can be regulated according to the frequency deviation. As the frequency drops, the DC-link voltage decreases, and the DC capacitors release the stored energy to the grid.

The system scheme in [65] is shown in Fig. 29. It is noted that the inertia support provided by the DC capacitors is limited. Thus, the OWF also needs to participate in FR. The DC voltage is used to transmit the grid frequency information to the WFVSC. The controller for adjusting the WFVSC frequency [65] is expressed as:

$$f_{WF}^* = f_{WF0} + K_B\left(V_{DC} - V_{DC0}\right) \tag{46}$$

When selecting the gain K_B, the DC voltage should be limited within $\pm 10\%$ of the nominal value. To regulate the output power of the OWF, the frequency–power droop control is applied by:

$$P_{WF}^* = P_{WF0} + \frac{1}{R}\left(f_{WF0} - f_{WF}\right) \tag{47}$$

where P_{WF0} is the nominal active power from the WF. Therefore, the GEC controller (45) with (46) and (47) can be used to coordinate the OWF and the VSC-HVDC to provide frequency support.

H. ADAPTIVE FREQUENCY REGULATION METHOD

Although a VSC-HVDC-based OWF can provide inertia support to improve frequency stability, WTs need to reduce their output power and absorb the required power to restore the rotor speed after a grid disturbance, which causes a power imbalance throughout the rotor speed recovery. Additional active power must be injected to compensate for the power shortage. Otherwise, a significant SFD may occur. To resolve the potential risk, [67] proposed a strategy that uses the permanent power reserve of the deloaded WTs to offset the power shortage during the rotor speed recovery of the WTs. The proposed strategy is called adaptive frequency regulation (AFR) [67], which is based on real operating conditions. The WTs can adaptively provide the releasable kinetic energy according to the rotor speed. In addition, the VSC-HVDC can also release the stored electrostatic energy according to the DC voltage to provide frequency support.

The control scheme proposed by [67] is shown in Fig. 30. Owing to the decoupling of the VSC-HVDC, the OWF cannot detect frequency disturbances. However, the sequential droop control strategy can be employed to achieve coupling between the OWF and the grid. It is expressed by:

$$P_G = P_{G0} - K_G\left(f - f_0\right) \tag{48}$$
$$V_{DC} = V_{DC0} + K_A\left(f - f_0\right) \tag{49}$$
$$f_{WF} = f_{WF0} + K_B\left(V_{DC} - V_{DC0}\right) \tag{50}$$
$$P_{WF} = P_{WF0} - K_{WF}\left(f_{OWF} - f_{OWF,0}\right) \tag{51}$$

where K_G, K_A, K_B and K_{WF} are the droop coefficients of the onshore SGs, GSVSC, WFVSC and OWF, respectively; P_{G0} and P_{WF0} are the nominal values of the output power of onshore SGs and OWFs, respectively, and f_0 and f_{WF0} are the nominal frequencies of the onshore grid and the OWF, respectively.

In previous studies, the parameters for the FR are almost constant. However, the releasable kinetic energy stored in the WT's rotor and the electrostatic energy stored in the DC capacitors are time-varying according to their operating statuses. The releasable kinetic energy, μ, and the electrostatic energy, ν, are defined as [68]:

$$\mu = \frac{J_{WT}\omega_t^2 - J_{WT}\omega_{t,min}^2}{J_{WT}\omega_{t0}^2 - J_{WT}\omega_{t,min}^2} = \frac{\omega_t^2 - \omega_{t,min}^2}{\omega_{t0}^2 - \omega_{t,min}^2} \tag{52}$$
$$\nu = \frac{CV_{DC}^2 - CV_{DC,min}^2}{CV_{DC0}^2 - CV_{DC,min}^2} = \frac{V_{DC}^2 - V_{DC,min}^2}{V_{DC0}^2 - V_{DC,min}^2} \tag{53}$$

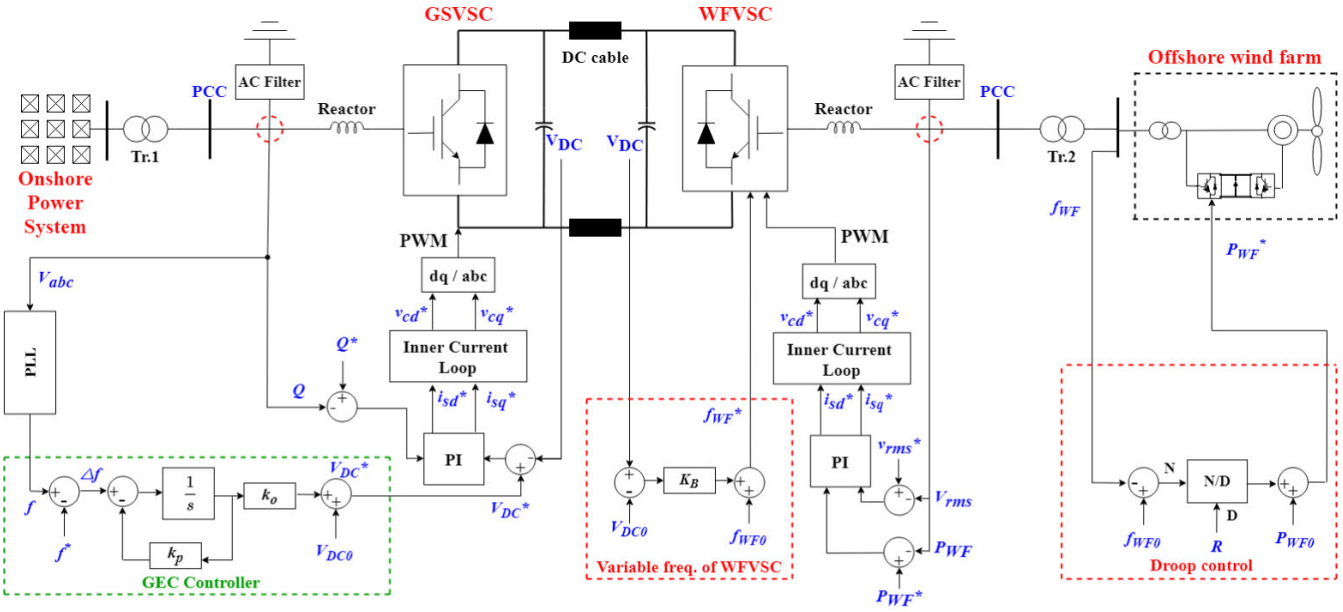

FIGURE 29. The schematic diagram of the GEC for VSC-HVDC connected WF.

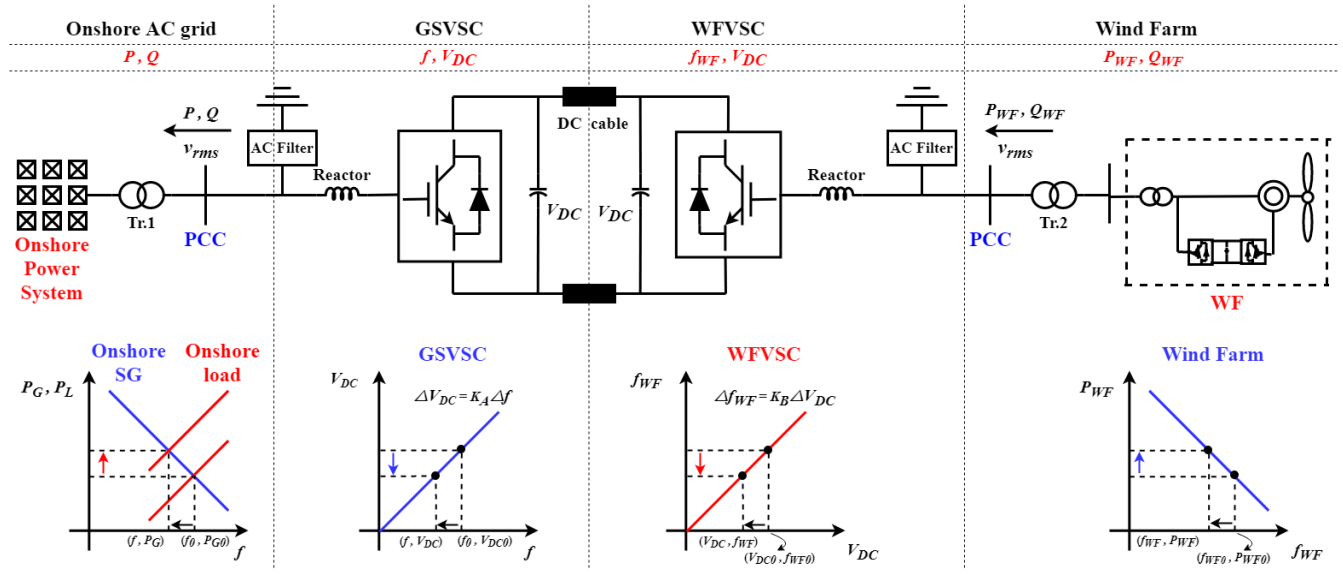

FIGURE 30. The schematic diagram of the adaptive frequency regulation (AFR) method.

where J_{WT} is the moment of inertia of the WT; ω_t is the rotor speed; $\omega_{t,min}$ is the minimum rotor speed; ω_{t0} is the nominal rotor speed; C is the DC capacitor value; $V_{DC,min}$ is the minimum DC voltage, and V_{DC0} is the nominal DC voltage.

For the frequency controllers of the WTs, the inertial gain k_{in} and the droop gain k_f are calculated according to the releasable kinetic energy μ as expressed in (54) and (55), and the additional output power of inertial control ΔP_{in} and droop control ΔP_f are expressed by (56) and (57), respectively.

$$k_{in} = k_{in0} \cdot \mu \tag{54}$$

$$k_f = k_{f0} \cdot \mu \tag{55}$$

$$\Delta P_{in} = -k_{in} \frac{df}{dt} \tag{56}$$

$$\Delta P_f = -k_f (f - f_0) \tag{57}$$

where k_{in0} and k_{f0} are the gains of inertial control and droop control at the rated speed, respectively.

The rotor speed recovery can be achieved by a PI controller, as expressed by (58), where ω_{t0} is the initial rotor speed and k_ω^p and k_ω^i are the proportional gain and the integral gain of the PI controller, respectively. Hence, the reference of the output power from the WTs with continuous rotor speed recovery,

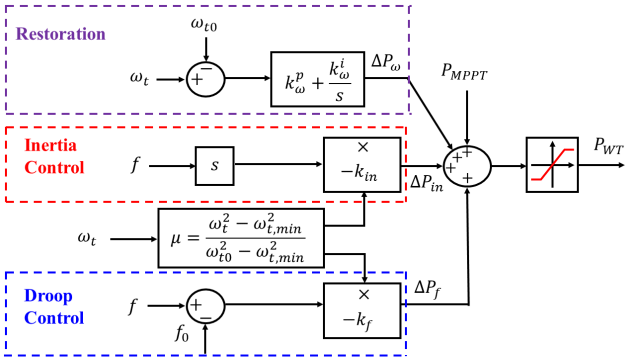

FIGURE 31. The output active power of the WTs providing primary frequency support by using AFR control.

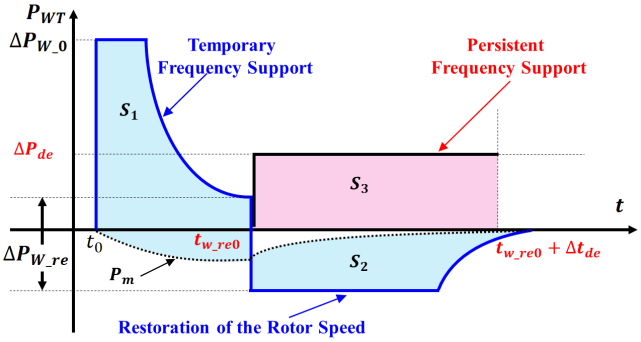

FIGURE 32. The coordination between the WTs in AFR control.

P_{WT}, is expressed as (59) and shown in Fig. 31 [67].

$$\Delta P_\omega = k_\omega^p (\omega_t - \omega_{t0}) + k_\omega^i \int (\omega_t - \omega_{t0})\, dt \tag{58}$$

$$P_{WT} = P_{MPPT} + \Delta P_{in} + \Delta P_f + \Delta P_\omega \tag{59}$$

The deloaded WTs provide a persistent power reserve for offsetting the power shortage during rotor speed recovery to provide temporary frequency support and electrostatic energy recovery for the VSC-HVDC. As shown in Fig. 32, the area S_1 represents the released energy during the temporary frequency support and the area S_2 represents the absorbed energy during the rotor speed recovery, defined, respectively, as:

$$S_1 = \int_{t_0}^{t_{W\_re0}} (P_{WT} - P_m)\, dt \tag{60}$$

$$S_2 = \int_{t_{W\_re0}}^{t_{W\_re0}+\Delta t_{de}} (P_m - P_{WT})\, dt \tag{61}$$

where P_{WT} and P_m are the electrical power and the mechanical power of the WTs, respectively; t_0 is the initial time of the frequency event; t_{W_re0} is the initial time of the rotor speed recovery, and Δt_{de} represents the duration of the recovery stage. According to the law of conservation of energy, S_1 equals S_2.

The persistent energy reserve provided from the deloaded WTs must exceed the energy absorbed by other WTs and the VSC-HVDC, which is expressed by:

$$S_3 = \int_{t_{W\_re0}}^{t_{W\_re0}+\Delta t_{de}} \Delta P_{de} dt \tag{62}$$

$$S_3 \geq S_2 \tag{63}$$

Notably, only a few WTs in commercial OWFs operate in the deloaded mode. Most WTs operate in MPPT mode. Thus, the use of deloaded WTs is a disadvantage of the adaptive strategy.

To illustrate the differences between the FR techniques introduced in this section, a comprehensive comparison of these strategies is shown in TABLE 1.

It is hard to tell which FR technique is the best. Every technique has its own advantages and drawbacks. Take the conventional scheme and the cascading control for example, cascading control can achieve a higher wind harvest, but it requires a larger deviation of the DC-link voltage, which may require a larger capacitance or may violate the DC-link voltage threshold when providing the inertia support. In contrast, the conventional scheme does not guarantee the high wind harvest nor the large deviation of the DC-link voltage. Therefore, it is a trade-off between the economic profits from the wind energy and the normal range of the DC-link voltage when using the cascading control.

IV. SIMULATION RESULTS

To validate the control methods described in Section III, this paper implements these methods by PSCAD/EMTDC. The parameters of the VSC-HVDC-connected WF model are shown in TABLE 2. An aggregated generic model of WTs is built to represent a WF in the simulation. An SG is tripped off at t = 10s to simulate an under-frequency event.

A total of eight methods were discussed in Section III. However, only the typical methods were selected for performing the simulation. The study cases are described in TABLE 2. Throughout the simulation, a deloaded WF is connected to the same bus where a WF provides frequency support based on the AFR strategy.

Case 1 is assumed to be the worst case, owing to the lack of frequency support from both VSC-HVDC and WF. In Fig. 33 (a), the frequency in Case 2 has a higher frequency nadir than Case 1, because the WF provides frequency support in which the grid frequency is transmitted through a communication channel to the WF. In Fig. 33 (b) and Fig. 33 (c), the frequency at the WF side and the DC-link voltage in Case 2 are kept constant throughout the simulation because the conventional scheme does not activate the inertia support from VSC-HVDC. By contrast, in Fig. 33 (a), the frequency with simultaneous control has an SFD caused by the reduction of output power from the WF. The output power from the WF using simultaneous control is the maximum among all cases. Nevertheless, in Fig. 34 (a) and Fig. 34 (b), the output power from the WF using simultaneous control is so large that the rotor speed of the WTs drops quickly. The output power of WTs for providing frequency support mainly comes from the stored kinetic energy in the rotor. Thus,

TABLE 1. Comparative analysis of various FR strategies for VSC-HVDC integrated WF.

No.	Control Method	Operation	Advantage	Disadvantage	Ref.
1.	Conventional Scheme	• f is directly transmitted to the WFVSC	• Very simple process	• Time delay may cause the inferior performance	[48]
2.	Simultaneous Control	• Transformation of Δf into ΔV_{DC}	• Without having to exchange information for the WF	• The rotor speed of WT deviates from the optimal value, causing the lower wind harvest	[48], [51] - [53]
3.	Inertial Emulation Control	• Assuming an emulated inertia constant H_{VSC} for VSC-HVDC	• The inertia constant can be specified and varied according to the performance requirements.	• ΔV_{DC} can be very large if a large H_{VSC} or a small C	[55] - [58]
4.	Blending Control of the VSC-HVDC and the WF for Fast Frequency Regulation	• Assuming an emulated inertia constant H for VSC-HVDC • Using a designated time constant to determine the frequency support from VSC-HVDC and WF	• Neither requirement of the large capacitance nor the high-performance WTs	• The benefits would be lost if very fast reaction time of the WF is required	[60]
5.	Modified VSC Control with Ancillary Frequency Controller	• m_a for implementing the PWM at WFVSC is determined by V_{WF} • Transmitting f to the WFVSC	• The behavior of f_{WF} can be very similar to that of f	• The latency of WF responding to Δf weakens the strength of FR	[46]
6.	Cascading Control	• Communication between GSVSC and WFVSC • VSC-HVDC takes precedence over WF	• Guaranteeing harvesting wind energy • The smaller of the deviation of ω_t of WTs	• Requirement of a very large DC capacitance • V_{DC} easily reaches V_{max} or V_{min}	[63]
7.	Generator Emulation Control	• V_{DC}^* is determined by Δf passing through a PLL	• Larger synthetic inertia with smaller DC capacitance can be provided by coordinating the FR of WF	• Requirement of a larger DC capacitance for a larger synthetic inertia	[64] [65]
8.	Adaptive Frequency Regulation	• Extracting the releasable energy and the KE stored in the DC capacitors and the WF • Restoring the rotor speed of WTs by using the energy from the other deloaded WTs	• The VSC-HVDC and the WF can be kept in the safe operation	• Using the deloaded WTs is not an economic choice	[67] [68]

the higher the rotor speed, the more the additional active power the WTs can provide. Although the rotor speed does not violate the minimum limit in Case 3, the output power is still slowly reduced because of the decrease of kinetic energy stored in the rotor.

The DC-link voltage is depicted in Fig. 33 (c). As described in Section III F, the frequency support from WF is activated only when the DC-link voltage reaches the limits. Therefore, the DC-link voltage in Case 4 drops the most among all cases. Furthermore, as the DC-link voltage recovers, the frequency at the WF side in Case 4 also starts to recover. Once the frequency returns to the nominal value, the frequency support from the WF stops and the output of the WF is lower than the pre-fault value to restore the rotor speed. In Fig. 34 (b), the rotor speed of WTs with cascading control has the smallest reduction and the fastest recovery. As a result, the cascading control ensures less wind energy loss compared to other methods.

The frequency response in Case 5 outperforms other cases. The difference between Case 3 and Case 5 is that the SFD is eliminated in Case 5. The frequency in Case 5 can be stabilized by an additional power from the deloaded WTs, as shown in Fig. 34 (c). Unlike Case 3, the SFD is avoided in Case 5, because the deloaded WTs managed to offset the power shortage during rotor speed recovery. The pre-defined rotor speed profile of the deloaded WTs is shown in Fig. 34 (d). As discussed in Section II-B, the power margin x of the deloaded WTs is set to 10% by using the overspeeding technique. The output power of the deloaded WTs cannot be increased immediately when the fault occurs

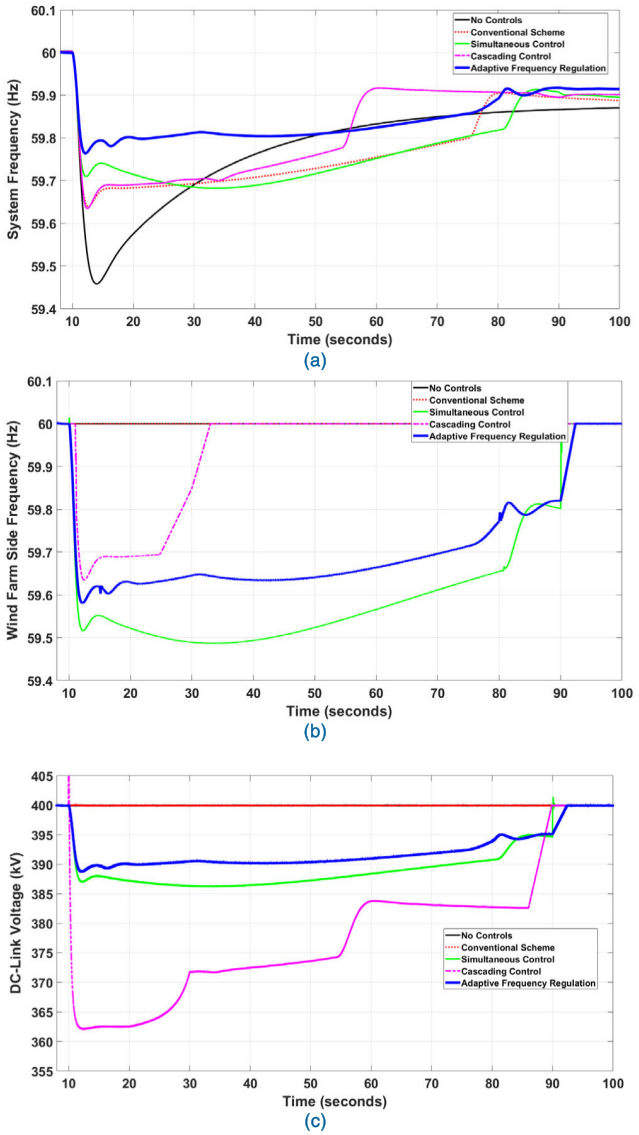

FIGURE 33. Simulation results for a SG trip-off. (a) System frequency. (b) Wind farm side frequency. (c) DC-Link voltage.

because the output power is decreased with the reduction of rotor speed, which contradicts the goal of providing an energy reserve. As a result, the output power of the deloaded WTs drops slightly during the transient period.

To further investigate the validity of the above methods, various important metrics are summarized in TABLE 3. It shows that simultaneous control yields the largest active power delivered by the WF. However, this large active power causes significant rotor speed deviation. Therefore, the SFD is more severe than the first frequency drop, and the corresponding time to reach the frequency nadir, Δt_{nadir}, is much longer than in other cases. In addition, the frequency metrics between Case 2 and Case 4 are similar, but Case 4 demonstrates a better rotor speed response for the WTs, as shown in Fig. 34 (b). With the assistance of the deloaded WTs, the output power of the WTs for providing frequency support lasts for an adequate amount of time and remains at a high

TABLE 2. Parameters of the simulated VSC-HVDC connected WF system.

Parameters	Values
Nominal AC frequency	60 Hz
Rated grid AC rms voltage	420 kV
Rated VSC power	300 MVA
Nominal DC-link voltage	400 kV
DC-link voltage range	0.9 – 1.1 p.u.
DC-link capacitors	0.25 mF × 2
Fixed load	300 MW
Rated power of WF	140 MW
Rated power of deloaded WF in adaptive frequency regulation	115 MW
Rotor speed range of WTs	0.6 p.u. – 1.2 p.u.
Rated wind speed	12 m/s
wind speeds for WF providing frequency support and deloaded WF	10 m/s and 8.5 m/s
Inertial gain $K_{inertia}$ and droop gain R of WTs	25 and 0.025
DC-link recovery time	86 – 90 s

TABLE 3. Study cases.

Case	Description
1	Without any frequency control
2	Conventional scheme (only frequency support from WF)
3	Simultaneous control (frequency support from VSC-HVDC and WF)
4	Cascading control (frequency support from VSC-HVDC and WF)
5	Adaptive frequency regulation (frequency support from VSC-HVDC and WF) with deloaded WTs

level in Case 5. It can be seen that the frequency nadir and the steady-state frequency in Case 5 are the highest. Consequently, the frequency metrics in Case 5 are the best among all cases.

Nonetheless, each method has its benefits and drawbacks. In fact, it is difficult to obtain a single optimal strategy. For example, the inertial gain and droop gain of WTs should be selected carefully to prevent excessive output power from the WTs when using simultaneous control. In terms of the cascading control, the rotor speed recovery of WTs is the fastest, but the DC-link voltage drops to the minimum limit. In terms of the deloading strategy, it is not an economic choice for commercial WFs, although the frequency response with AFR is the most efficient.

V. FREQUENCY REGULATION STRATEGIES FOR WTs AND ESSs

With the increasing penetration of renewable energy, grid frequency stability is facing serious challenges. Many grid

TABLE 4. Frequency metrics and the WF responses for different cases.

Case	Δt_{nadir} (s)	Frequency Nadir (Hz)	ROCOF (Hz/s)	Settling Time (s)	Steady State Frequency (Hz)	Minimum Rotor Speed (pu)	Minimum WF Power (MW)	Maximum WF Power (MW)
1	13.9726	59.4586	-0.2898	90	59.8704	1.0872	83.32	83.42
2	12.6153	59.6397	-0.2730	96	59.8885	0.8719	73.42	106.35
3	33.7768	59.6825	-0.2489	98	59.8963	0.8059	73.70	114.01
4	12.4365	59.6350	-0.2645	92	59.9021	0.9022	70.64	106.98
5	12.1242	59.7638	-0.2034	90	59.9146	0.8493	74.13	110.20

codes have requested renewable energy resources to provide a fault ride through capability [69]. If ESSs can contribute to the ancillary services in power systems, then frequency stability can be further improved. Thus, the ESS has become an important role. This study conducted a comprehensive comparison of different FR strategies by WTs and ESSs.

Traditionally, the control methods of ESSs used to provide FR are generally based on inertial control and droop control. In [70], the authors validated the virtual inertia of the BESS by deploying an inertial controller in its energy management system. The inertia in a high wind penetration system is increased if the BESS has a significantly large capacity. The authors of [71] applied a lead-lag controller to control the BESS for stabilizing the system frequency. The lead-lag controller is used to control the output power by adjusting the d-axis and q-axis currents of the inverter of the BESS. The BESS with lead-lag controller outperforms that with a traditional PI controller for minimizing the frequency disturbance with increased wind penetration.

For advanced control, [72] utilized the fuzzy logic controller to control the output power of the ESS for providing frequency support. The reference power of the ESS is determined by fuzzy logic. The inputs of the fuzzy controller are the frequency deviation and the ROCOF, and the output is the reference power of the BESS. For example, if the frequency deviation is negative and large, then the reference power should be large and last for a long period to supply the required energy. If the frequency deviation is negative and small, and the ROCOF is positive and small, then the frequency would slowly increase to the nominal value and the reference power of the BESS would be not too large.

The power reserve can be quickly injected to the network if the WTs are operating in deloaded mode. The hybrid operation of deloaded WTs and the BESS ensures the power balance between supply and demand during a load variation [73]. The fast response of the BESS combined with the power reserve of the WTs can significantly improve the FR capability. The coordination between the level of the power margin of the deloaded WTs and the reference power of the FESS is discussed in [74]. In this coordinated strategy, the deloading operation of WTs can be avoided if the power margin can be handled by the FESS, which means the FESS is prioritized for providing frequency support. This method enables WTs to maintain sufficient power reserve while alleviating the need for the deloading operation.

The ESS can also help to maintain the constant output power of WTs. In [75] and [76], a supercapacitor is installed in the DC-link of a WT for alleviating the power fluctuation. The WT with a supercapacitor can be seen as a combined wind source that is always operating in MPPT mode. When there are wind speed variations and load steps, the supercapacitor can absorb or release active power to stabilize the system frequency, while keeping the WTs in MPPT operation. The installment of an ESS in the DC-link can also be applied to the VSC-HVDC system for mitigating power fluctuation and limiting the fault current [77]. Considering the transient state when the fault occurs, the superconducting coil and the flywheel are suitable for provide fault ride through support, owing to their fast response. The aim is to minimize the DC-link voltage deviation and fault current, as presented in the optimization problem in [78].

The frequency-control algorithm of the ESS and WF can be designed as a step-by-step strategy. A two-stage FR strategy was developed in [79]. In the first stage, wind speed is predicted to determine the reference power for the ESS. The ESS is only activated when the capacity of SGs is insufficient for mitigating the frequency disturbance. Then, the actual frequency deviation is measured to modify the reference power of the ESS in the second stage. In this two-stage strategy, the life of the ESS can be prolonged because the frequent charging and discharging cycles are prevented. Additionally, the duration of the FR process can be shortened, as the ESS is prepared in advance by predicting the wind power disturbance. In contrast, a three-stage coordinated control strategy among the WF, BESS and conventional SGs was proposed in [80]. The first stage is activated when a serious frequency drop is detected, and the WTs will perform the torque limit control to provide frequency support. In the second stage, the PMSGs switch to the deloading operation to prepare for the rotor speed recovery and the BESS will replace the WTs for providing frequency support. Finally, if the system frequency decreases to a specified value, then conventional

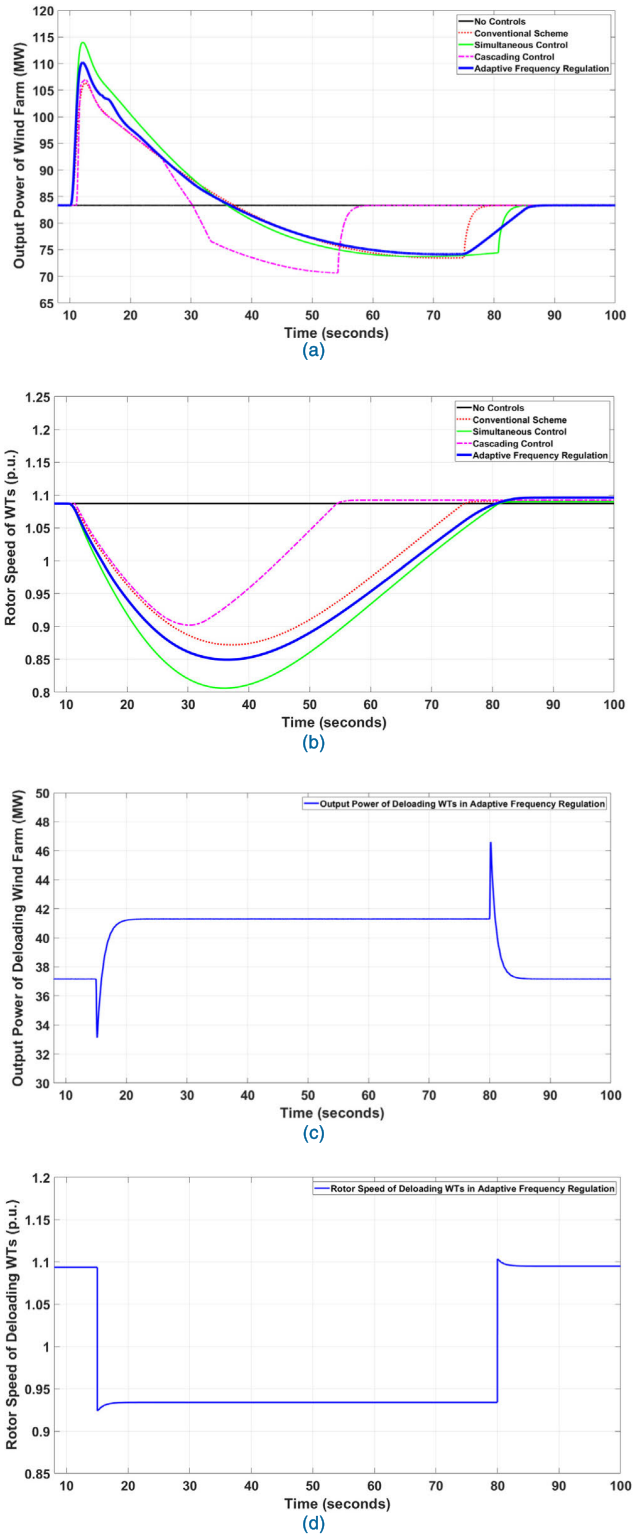

FIGURE 34. Simulation results for a SG trip-off. (a) Output power of WTs for providing frequency support. (b) Rotor speed of WTs for providing frequency support. (c) Output power of deloaded WTs. (d) Rotor speed of deloaded WTs.

SGs with power reserves can boost their output power to the grid. This strategy effectively improves the frequency response and avoids an SFD during the rotor speed recovery of the WTs.

In [81], a strategy based on superconducting magnetic energy storage (SMES) was proposed to compensate the required power for the generator rotor speed recovery of WTs. In principle, a VSC-HVDC-connected OWF with ESSs was capable of exhibiting good performance for providing frequency support. Reference [82] proposed an FR strategy by using the power reserve of deloaded WTs and the fast response of SMES to alleviate the burden of the diesel generator.

Typically, the types of ESSs can be classified into two categories according to their power and energy characteristics. The first category is high power density (e.g. supercapacitors, flywheels, SMES, etc.), and the other is high energy density, e.g., batteries. An ESS with high power density can absorb or inject a large amount of power within a very short period of time, especially for providing virtual inertia in a few seconds. By contrast, an ESS with high energy density can provide primary or secondary FR by sustaining its output power for a longer period, up to tens of minutes.

Utilizing hybrid types of ESSs for providing frequency support has been investigated in some studies [83]–[86]. Commonly, there are at least one high-power-density ESS and one high-energy-density ESS in hybrid operation. For example, the job of a supercapacitor is to deal with the high-frequency components or rapidly changing signals in the grid, while leaving low-frequency components or smooth signals for the BESS. The supercapacitor can absorb the ripple in power systems and help prevent the BESS from operating with a high depth-of-discharge (DOD) rate; thus, the life of the battery is extended.

When adding the ESS into the network for providing frequency support, the state of charge (SOC) of the ESS should be carefully considered. A SOC value of 50% was reported to be the optimal working point of the BESS in [87]. The SOC can be maintained at approximately 50% by using the SOC feedback control proposed by [87]. The pitch angle control of WTs and the droop control of SGs can be activated to mitigate the frequency disturbance when the SOC of the BESS exceeds the limitations. Improved droop control based on SOC was investigated in [88] and [89]. The droop gain can be adaptively changed according to the current value of SOC. That is, the higher the SOC, the more power the ESS can generate and vice versa. The level of SOC has a tremendous impact on battery lifetime, when it is used to provide primary frequency support. Consequently, the revenues for the Li-ion BESS were analyzed in [90]. The simulation results show that the primary frequency support strategy from ESSs should be carefully designed to avoid rapid deterioration in order to achieve a good economic profit.

The size of the ESS plays a crucial role, especially when considering the installation of the ESS to increase the system inertia. The size of the ESS can be determined according to the targeted frequency dynamics [91]. The proposed method in [91] estimates the size of the ESS in terms of the power shortage, so as to achieve the target inertia constant and the power/frequency characteristics. Additionally, the sizing

is calculated for inertial response and primary frequency response.

VI. FUTURE TRENDS

A. OPTIMIZATION OF COORDINATED CONTROL OF FREQUENCY REGULATION TECHNIQUES FOR VSC-HVDC-INTEGRATED WFs AND ESSs

To improve the robustness and reliability of the coordinated frequency control strategy under different frequency events, cooperation among the conventional SGs, renewable energy sources (RESs), and ESSs is required. The allocations of the amounts of generation among the conventional SGs, RESs, and ESSs for providing FR can be made based on the installation capital operation costs, lifespan, and system requirements. Furthermore, the precedence, duration, and ramp-up rate should be taken into consideration when implementing the IR, PFR, SFR, and TFR for different power reserves. Therefore, the need for research into optimization is urgent and essential. Additionally, different wind penetrations, variable wind-speed scenarios, and realistic cases should be taken into account when performing such analysis.

An optimal control strategy called model predictive control (MPC), which uses state-space predictions, has been popularly investigated in recent years. The adaptive MPC was utilized for load frequency control (LFC) in [92] and [93]. The adaptive MPC can minimize the frequency deviation in the presence of load disturbance. The weights of the cost functions of traditional MPC are chosen by trial-and-error in several simulation cases. By contrast, the adaptive MPC can tune the dynamic parameters based on the real conditions automatically. Consequently, the adaptive MPC displays greater robustness and reliability than the traditional MPC and PID controller in terms of the FR capability.

For advanced control, the MPC can be utilized for the LFC of a multi-area power system that suffers from malicious cyber attacks [94]. It reveals that more severe cyber-attacks such as denial of service (DoS) or deception attacks are worthy of research in detail, especially in high-tech power systems.

References [95], [96], [97] presented control strategies for an MPC providing LFC in a system containing an ESS. The authors of [97] demonstrated that the MPC can help reduce the capacity and energy of an ESS compared to a traditional PI controller. Another example of MPC for FR considering the power constraints of an ESS was proposed in [98], in which the optimal power allocation of an ESS was achieved in a tested real Taiwan power system. The applications of MPC for AC voltage and FR in the case of RES power variation and load disturbance in microgrids can be found in [99], [100], [101].

MPC can also be employed for coordinating the AGC for FR and DC power regulation in multi-terminal HVDC (MTDC) grids [102], [103]. Moreover, the communication delays and DC voltage constraints were considered when implementing the AGC in [104] and [105]. It is recommended that the nonlinear/adaptive MPC be further applied for the realistic model of a large-scale power system, e.g., the European super grid.

Some other optimization methods have been proposed in [106], [78]. The authors of [106] proposed a low-order response model for presenting the WF-MTDC participating in FR. This model helps establish the appropriate variation of DC-link voltage and frequency deviation for MTDC by setting the droop gain. In [78], the author proposed an optimization strategy for installing SMES in the DC-line of HVDC for alleviating wind power fluctuation and providing a fault-current-limiting capability. The optimal problem aims to minimize the DC power deviation, DC-link voltage fluctuations, the initial inductance and the initial current of the SMES. The optimal SMES needs less power and energy than non-optimal SMES when suppressing the fault current. Thus, the economic benefit is achieved.

Aside from the MPC algorithms, there are some advanced optimization frequency control strategies based on artificial neutral networks (ANNs), machine learning, generic algorithm and so on. Reference [107] calculated the optimal electrical frequency for an offshore WF to generate the maximum power during a normal operation. By contrast, the output power of a WF is reduced when a voltage disturbance occurs in the HVDC link, which corresponds to a fault at the onshore AC grid. The authors in [108] proposed an iterative procedure to compute the optimum parameters for supporting the fault ride-through capability of a VSC-HVDC-connected WF by using the mean variance mapping optimization (MVMO) algorithm. The developed meta-heuristic algorithm can provide the best solution to minimize the DC over-voltage. In addition, the frequency of WF can be regulated based on the DC-bus voltage, and the dynamic response of the VSC-HVDC-connected offshore WF can be improved by using the proposed evolutionary optimization algorithm. An adaptive droop control was proposed for frequency regulation in a VSC-multi-terminal DC (VSC-MTDC) system [109]. Additionally, a voltage-current-frequency characteristic was also proposed to autonomously redistribute the power sharing among all the grid-side VSCs (GSVSCs). Significantly, the optimal parameters for the adaptive droop control were obtained by carrying out the modal analysis and nonlinear simulations; thus, the frequency deviation can be minimized. The authors in [110] studied the integration of a WF into a VSC-MTDC system for load frequency control. A traditional objective function called integral time absolute error (ITAE) cannot decrease the overshoot of the system response. To resolve this problem, a modified objective function was proposed, in which the control parameters for all generation units and the modified objective function are determined by particle swarm optimization (PSO) algorithm. Moreover, the multiple constraints were considered in [110] to investigate a more realistic power system. The performance of the load frequency control by using the proposed advanced control is greatly improved. In [111], the authors investigated the virtual inertia control for the wind energy conversion

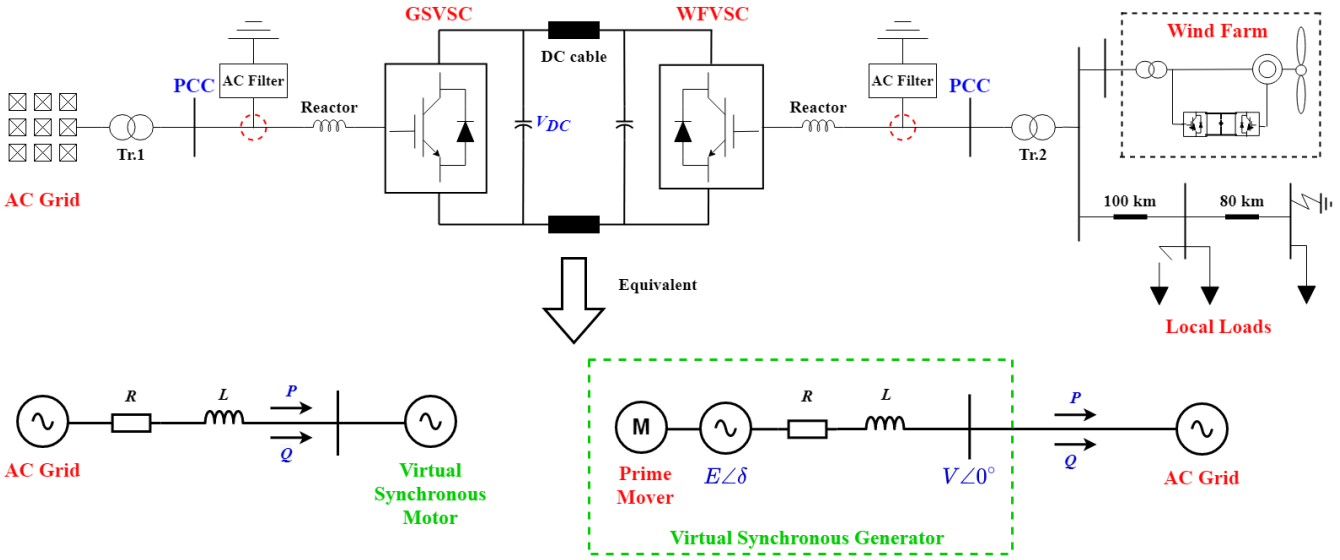

FIGURE 35. The schematic diagram of the VSM for a VSC-HVDC system. The left AC grid is the strong grid; while the right WF and the local loads form the weak grid.

system (WECS). A novel optimization control called artificial bee colony (ABC) algorithm was applied to calculate the optimal gain for the virtual inertia control of WTs. The proposed control strategy was tested in a multi-area system containing a VSC-HVDC, and the simulation results demonstrated that a high frequency stability and a low power deviation are achieved. Reference [112] proposed a coordinated frequency control strategy based on situation awareness (SA) for achieving the dynamic adjustment of the parameters of the frequency controller. The SA can automatically change the controller settings by monitoring the on-line operations, and it is divided into perception, analysis and prediction stages. By applying the SA in frequency regulation, the optimal performance can be obtained.

For a VSC-HVDC-integrated-WF system, traditional advanced optimization algorithms rarely consider energy storage systems (ESSs) for providing frequency support. The ESSs have numerous benefits for providing ancillary services. Hence, the interaction between them can be further studied in the future work.

B. VIRTUAL SYNCHRONOUS MACHINE TECHNIQUE FOR A WEAK AC SYSTEM

As the penetration of non-synchronous generation increases, the system inertia and strength are correspondingly reduced. The ability of a PLL to synchronize with the main grid loses accuracy when the short-circuit ratio (SCR) is less than 1.3, which is a possible value for a microgrid or a weak AC grid [113]. A virtual synchronous machine (VSM) was proposed as an alternative to PLL when the VSC is connected to the grid. The VSM is viewed as a potential solution for the next generation of grid-connected converters, especially for an islanded microgrid or an extremely weak grid [114], [115], [116]. The main idea of VSM is to emulate the electromagnetic equations and the rotor motion of conventional synchronous machines. Typically, there are two forms of VSM: a virtual synchronous generator (VSG) with a synchronous inverter [117]–[119] and a virtual synchronous motor – with a synchronous rectifier [120], [121]. A schematic diagram of a VSM for a WF and local loads connected to the main grid via VSC-HVDC is depicted in Fig. 35. Most literature has focused on the VSG for providing frequency support.

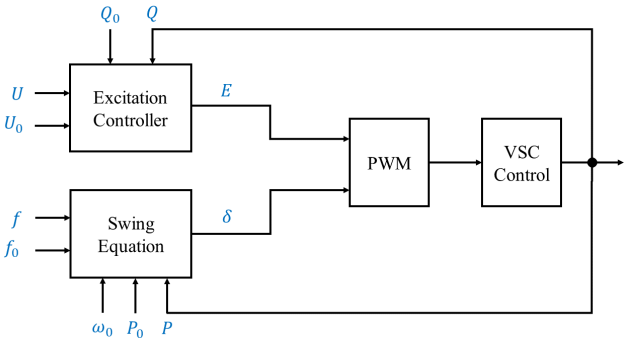

FIGURE 36. The basic control structure of the VSG.

The basic control structure of the VSG is shown in Fig. 36. The active power adjustment of VSM relies on the $P-f$ droop characteristic and the swing equation as shown in Fig. 37, while the output reactive power depends on the $Q-V$ droop characteristic, as shown in Fig. 38 [122], [123]. The VSG emulates the rotor motion equation and the excitation controller of a traditional SG as follows:

$$P_m = P_0 - K_f\,(f - f_0) \tag{64}$$

$$J\omega\frac{d\omega}{dt} = P_m - P - \omega\cdot D_p\,(\omega - \omega_0) \tag{65}$$

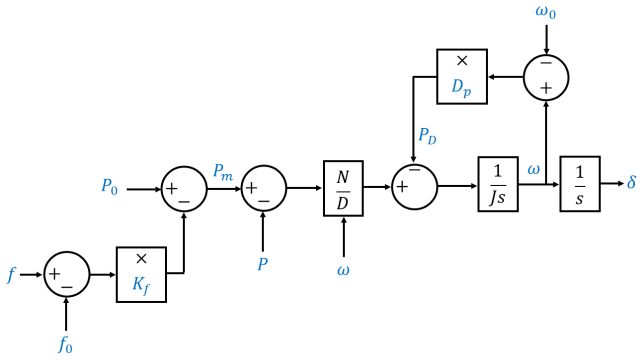

FIGURE 37. The control scheme of the active power-frequency controller of VSG.

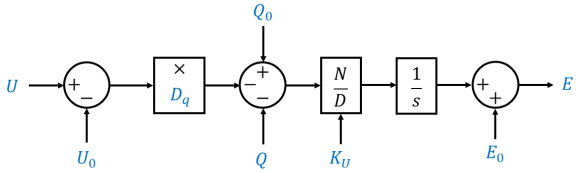

FIGURE 38. The control scheme of the reactive power-voltage controller of VSG.

$$E = \frac{1}{K_U}\int \left[Q_0 - Q - D_q\left(U - U_0\right)\right] + E_0 \quad (66)$$

where P_m is the mechanical input power, P_0 is the initial active power, K_f is the frequency coefficient, f_0 is the nominal frequency, J is the moment of inertia, P is the electrical power, D_p is the damping coefficient, ω_0 is the nominal angular frequency, E is the electromotive force, K_U is the voltage coefficient, Q_0 is the initial reactive power, Q is the electrical reactive power, D_q is the reactive power coefficient, U is the rms grid side voltage, U_0 is the nominal grid side voltage, and E_0 is the no-load electromotive force.

An example of VSG applied at a VSC-HVDC stations can be found in [124], where primary and secondary frequency controls were achieved using a VSG. In [125], the inverter of the VSC-HVDC acts like the VSG providing a reference angle for the weak AC grid. It is advised that the VSG be applied in a zero-inertia or low-inertia system for providing frequency support. The stability and dynamic performance of the MTDC integrated into a very weak AC system using VSG were analyzed in detail in [126]. A VSG control that can suppress the negative sequence voltage in the passive network with unbalanced loads can be seen in [127]. The various types of impedance of the VSM-based VSC-HVDC were studied using Bode plots and the Nyquist criterion in [128]. Reference [129] proposed an adaptive strategy for the adjustable moment of inertia for a VSG

Although these VSM strategies can achieve the frequency and AC voltage regulation capabilities for VSC-HVDC, none of them include the control mechanisms for both WF and ESS when providing frequency support. The importance of WF cannot be ignored when it is connected via VSC-HVDC. Therefore, it is vital to research the coordinated control strategy of VSMs for the VSC-HVDC integrated WF and ESS. Moreover, the frequency-control strategy of VSMs when a three-phase fault, voltage harmonics, and a voltage drop occur simultaneously in the grid is worthy of further study.

VII. CONCLUSION

As a result of the increasing penetration of wind power generation, the number of VSC-HVDC connected OWFs is increasing. Thus, both VSC-HVDC and WTs play very crucial roles in maintaining frequency stability. This study investigated and compared various FR techniques from WTs, VSC-HVDC, and ESSs. The contributions of this paper are summarized as follows:

- Most of previous overview papers have been about the FR techniques for only WTs or only VSC-HVDC. However, this paper provided a detailed review of coordinated frequency control techniques for VSC-HVDC-integrated WFs.
- Unlike other review papers, this paper not only presented a comprehensive comparison of the FR techniques but also implemented a time-domain simulation to further analyze the effectiveness of the selected FR techniques.
- This work introduced some methodologies for using an ESS to coordinate WTs to provide frequency support.
- This paper showed current challenges and provided recommendations for the future.

The FR strategies for a VSC-HVDC-connected WF can be divided into two categories: communication-based strategies and non-communication-based strategies. In communication-based strategies, the grid frequency signal is transmitted to the WFVSC or OWF through a communication channel. However, the performance of the communication-based strategy can be affected by the latency, which delays frequency support from the OWF. By contrast, the non-communication-based strategy can utilize an ancillary voltage controller [46], GEC controller [65] or sequential droop controller [67] at the VSC stations. The response from the OWF by the non-communication-based strategy may be slower than those by the communication-based strategy, owing to controller operations and switch delays.

In the simulation results, it was shown that the AFR strategy yielded the best performance. The frequency nadir of the AFR was increased by 0.1241 Hz compared to the conventional scheme, and the maximum ROCOF was reduced by 25.5%. The respective frequency metrics of AFR are the best among these FR control strategies, showing that it is necessary to develop such an adaptive or optimal control approach. Notably, the minimum WT rotor speed of cascading control is increased by 12% compared to simultaneous control. Cascading control has the largest value for the minimum WT rotor speed, which is good for preventing the SFD.

The SFD problem caused by the rotor speed recovery of the WTs has rarely been studied. However, it is definitely worthy of attention because an SFD can cause a severe frequency

nadir. To solve this issue, the rotor speed recovery of WTs should be properly designed using the energy stored in the DC-link capacitors of VSC-HVDC, the energy reserve of deloaded WTs, or the instant power of an ESS.

Several FR strategies, especially for the primary frequency response for WTs and ESSs, have been proposed. These strategies use supercapacitors, flywheels, and electrochemical batteries. Although secondary and tertiary frequency response strategies have seldom used WTs and ESSs, their importance cannot be ignored and the ancillary services provided by ESSs should be investigated further in the future.

REFERENCES

[1] P. Tchakoua, R. Wamkeue, M. Ouhrouche, F. Slaoui-Hasnaoui, T. Tameghe, and G. Ekemb, "Wind turbine condition monitoring: State-of-the-art review, new trends, and future challenges," *Energies*, vol. 7, no. 4, pp. 2595–2630, Apr. 2014.

[2] *Guide for the Development of Models for HVDC Converters in a HVDC Grid*, CIGRE, Paris, France, 2014.

[3] J. Morren, J. Pierik, and S. W. H. de Haan, "Inertial response of variable speed wind turbines," *Electr. Power Syst. Res.*, vol. 76, no. 11, pp. 980–987, 2006, doi: 10.1016/j.epsr.2005.12.002.

[4] M. Kayikçi and J. V. Milanovic, "Dynamic contribution of DFIG-based wind plants to system frequency disturbances," *IEEE Trans. Power Syst.*, vol. 24, no. 2, pp. 859–867, May 2009, doi: 10.1109/TPWRS.2009.2016062.

[5] M. Hwang, E. Muljadi, J.-W. Park, P. Sorensen, and Y. C. Kang, "Dynamic droop–based inertial control of a doubly-fed induction generator," *IEEE Trans. Sustain. Energy*, vol. 7, no. 3, pp. 924–933, Jul. 2016, doi: 10.1109/TSTE.2015.2508792.

[6] M. Kang, J. Lee, K. Hur, S. H. Park, Y. Choy, and Y. C. Kang, "Stepwise inertial control of a doubly-fed induction generator to prevent a second frequency dip," *J. Electr. Eng. Technol.*, vol. 10, no. 6, pp. 2221–2227, Nov. 2015, doi: 10.5370/jeet.2015.10.6.2221.

[7] Y.-Z. Sun, Z.-S. Zhang, G.-J. Li, and J. Lin, "Review on frequency control of power systems with wind power penetration," in *Proc. Int. Conf. Power Syst. Technol.*, Oct. 2010, pp. 1–8, doi: 10.1109/POWERCON.2010.5666151.

[8] P. Bresesti, W. L. Kling, R. L. Hendriks, and R. Vailati, "HVDC connection of offshore wind farms to the transmission system," *IEEE Trans. Energy Convers.*, vol. 22, no. 1, pp. 37–43, Mar. 2007, doi: 10.1109/TEC.2006.889624.

[9] F. Díaz-González, A. Sumper, O. Gomis-Bellmunt, and R. Villafáfila-Robles, "A review of energy storage technologies for wind power applications," *Renew. Sustain. Energy Rev.*, vol. 16, no. 4, pp. 2154–2171, May 2012, doi: 10.1016/j.rser.2012.01.029.

[10] Z. Liu, H. He, S. Jiang, H. Yu, and S. Xiao, "The effects of wind turbine and energy storage participating in frequency regulation on system frequency response," in *Proc. IEEE 5th Adv. Inf. Technol., Electron. Autom. Control Conf. (IAEAC)*, Mar. 2021, pp. 283–288, doi: 10.1109/IAEAC50856.2021.9391047.

[11] H. Zhai, L. Xu, W. Gong, Y. Yao, B. Xu, and N. Dong, "Frequency response strategy of Wind-storage-PEV collaborated system," in *Proc. 6th Asia Conf. Power Electr. Eng. (ACPEE)*, Apr. 2021, pp. 783–788, doi: 10.1109/ACPEE51499.2021.9436953.

[12] W. Xian, L. Rui, F. Liang, S. Donglei, L. Dong, and S. Yi, "Application of energy storage technology in frequency control of high proportion new energy power system," in *Proc. 6th Asia Conf. Power Electr. Eng. (ACPEE)*, Apr. 2021, pp. 853–857, doi: 10.1109/ACPEE51499.2021.9437021.

[13] L. Toma, B.-P. Dobrin, M. Sanduleac, A. Mazza, E. Bompard, D.-O. Sidea, C. Bulac, and N. Anton, "Fuzzy logic based battery energy storage system control for frequency containment," in *Proc. 12th Int. Symp. Adv. Topics Electr. Eng. (ATEE)*, Mar. 2021, pp. 1–6, doi: 10.1109/ATEE52255.2021.9425081.

[14] H. Liu, C. Zhang, X. Peng, and S. Zhang, "Configuration of an energy storage system for primary frequency reserve and inertia response of the power grid," *IEEE Access*, vol. 9, pp. 41965–41975, 2021, doi: 10.1109/ACCESS.2021.3065728.

[15] G. Meng, Q. Chang, Y. Sun, Y. Rao, F. Zhang, Y. Wu, and L. Su, "Energy storage auxiliary frequency modulation control strategy considering ACE and SOC of energy storage," *IEEE Access*, vol. 9, pp. 26271–26277, 2021, doi: 10.1109/ACCESS.2021.3058146.

[16] F. Calero, C. A. Canizares, and K. Bhattacharya, "Dynamic modeling of battery energy storage and applications in transmission systems," *IEEE Trans. Smart Grid*, vol. 12, no. 1, pp. 589–598, Jan. 2021, doi: 10.1109/TSG.2020.3016298.

[17] F. Sun, P. Li, S. Liu, J. Hao, H. Yang, S. Wang, and P. Ye, "Distributed energy storage aggregator for power system frequency control," in *Proc. Int. Conf. Intell. Comput., Autom. Syst. (ICICAS)*, Dec. 2020, pp. 203–206, doi: 10.1109/ICICAS51530.2020.00049.

[18] G. Xu, L. Xu, and J. Morrow, "System frequency support using wind turbine kinetic energy and energy storage system," in *Proc. 2nd IET Renew. Power Gener. Conf. (RPG)*, 2013, pp. 1–4, doi: 10.1049/cp.2013.1812.

[19] G. Shu-Feng, Z. Jie-Tan, A. Philip, H. Li-Li, and J. Jing, "A review of wind turbine deloaded operation techniques for primary frequency control in power system," in *Proc. China Int. Conf. Electr. Distrib. (CICED)*, Sep. 2018, pp. 63–71, doi: 10.1109/CICED.2018.8592549.

[20] Z. Wu, W. Gao, T. Gao, W. Yan, H. Zhang, S. Yan, and X. Wang, "State-of-the-art review on frequency response of wind power plants in power systems," *J. Mod. Power Syst. Clean Energy*, vol. 6, no. 1, pp. 1–16, Jan. 2018, doi: 10.1007/s40565-017-0315-y.

[21] N. Julius, J. N. Nderu, and G. K. Irungu, "Frequency control and virtual inertia emulation techniques for grid connected wind energy conversion systems—A review," in *Proc. IEEE AFRICON*, Sep. 2019, pp. 1–6, doi: 10.1109/AFRICON46755.2019.9133975.

[22] Y. Cheng, R. Azizipanah-Abarghooee, S. Azizi, L. Ding, and V. Terzija, "Smart frequency control in low inertia energy systems based on frequency response techniques: A review," *Appl. Energy*, vol. 279, Dec. 2020, Art. no. 115798, doi: 10.1016/j.apenergy.2020.115798.

[23] E. Riquelme, C. Fuentes, and H. Chavez, "A review of limitations of wind synthetic inertia methods," in *Proc. IEEE PES Transmiss. Distrib. Conf. Exhib. Latin Amer. (T&D LA)*, Sep. 2020, pp. 1–6, doi: 10.1109/TDLA47668.2020.9326180.

[24] P. Li, W. Hu, and Z. Chen, "Review on integrated-control method of variable speed wind turbines participation in primary and secondary frequency," in *Proc. IECON 42nd Annu. Conf. IEEE Ind. Electron. Soc.*, Oct. 2016, pp. 4223–4228, doi: 10.1109/IECON.2016.7794127.

[25] S. M. Muyeen, "Grid interfacing of a small scale DC-based wind farm using fuzzy logic controlled inverter system," in *Proc. 21th Int. Conf. Electr. Mach. (ICEM)*, Sep. 2010, pp. 1–6, doi: 10.1109/ICELMACH.2010.5607829.

[26] Z. Haibo, F. Gruson, D. Florez, and C. Saudemont, "Analysis of the influence of different cable modelling for DC series offshore wind farm," in *Proc. 18th Eur. Conf. Power Electron. Appl. (EPE ECCE Eur.)*, Sep. 2016, pp. 1–9, doi: 10.1109/EPE.2016.7695471.

[27] Y. Patel and A. Nasiri, "DC distribution system architecture and controls for wind power applications," in *Proc. IEEE Energy Convers. Congr. Expo. (ECCE)*, Sep. 2012, pp. 3493–3499, doi: 10.1109/ECCE.2012.6342317.

[28] P. Kou, D. Liang, Z. Wu, Q. Ze, and L. Gao, "Frequency support from a DC-grid offshore wind farm connected through an HVDC link: A communication-free approach," *IEEE Trans. Energy Convers.*, vol. 33, no. 3, pp. 1297–1310, Sep. 2018, doi: 10.1109/TEC.2018.2814604.

[29] R. Yang, G. Shi, X. Cai, and X. Zhang, "Voltage source control of offshore all-DC wind farm," *IET Renew. Power Gener.*, vol. 13, no. 16, pp. 2986–2993, 2019, doi: 10.1049/joe.2018.9292.

[30] C. Qu, Y.-H. Yan, F. Jiang, W.-C. Ge, Y.-N. Lu, and C. Liu, "VSG-based PMSG multi-machine parallel with DC droop control strategy," in *Proc. IEEE 9th Int. Power Electron. Motion Control Conf. (IPEMC-ECCE Asia)*, Nov. 2020, pp. 2917–2922, doi: 10.1109/IPEMC-ECCEAsia48364.2020.9367940.

[31] M. Yu, A. Dysko, C. D. Booth, A. J. Roscoe, and J. Zhu, "A review of control methods for providing frequency response in VSC-HVDC transmission systems," in *Proc. 49th Int. Universities Power Eng. Conf. (UPEC)*, Sep. 2014, pp. 1–6, doi: 10.1109/UPEC.2014.6934693.

[32] J. Fradley, R. Preece, and M. Barnes, "VSC-HVDC for frequency support (a review)," in *Proc. 13th IET Int. Conf. AC DC Power Transmiss. (ACDC)*, 2017, pp. 1–6, doi: 10.1049/cp.2017.0062.

[33] J. Wu, Z. Wang, H. Rao, Y. Chen, and W. Huang, "A review of control strategies for inertia support in VSC-HVDC system," in *Proc. 4th IEEE Workshop Electron. Grid (eGRID)*, Nov. 2019, pp. 1–6, doi: 10.1109/eGRID48402.2019.9092740.

[34] U. Tamrakar, D. Shrestha, M. Maharjan, B. P. Bhattarai, T. M. Hansen, and R. Tonkoski, "Virtual inertia: Current trends and future directions," *Appl. Sci.*, vol. 7, no. 7, p. 654, 2017, doi: 10.3390/app7070654.

[35] A. Junyent-Ferré, O. Gomis-Bellmunt, A. Sumper, M. Sala, and M. Mata , "Modeling and control of the doubly fed induction generator wind turbine," *Simul. Model. Pract. Theory*, vol. 18, no. 9, pp. 1365–1381, Oct. 2010, doi: 10.1016/j.simpat.2010.05.018.

[36] F. Díaz-González, M. Hau, A. Sumper, and O. Gomis-Bellmunt, "Participation of wind power plants in system frequency control: Review of grid code requirements and control methods," *Renew. Sustain. Energy Rev.*, vol. 34, pp. 551–564, Jun. 2014, doi: 10.1016/j.rser.2014.03.040.

[37] *Load-Frequency Control and Performance*, Operations Reports, ENTSO-E, Brussels, Belgium, Apr. 2009. [Online]. Available: https://eepublicdownloads.entsoe.eu/clean-documents/pre2015/publications/ce/oh/Policy1_final.pdf

[38] *Operational Limits and Conditions for Mutual Frequency Support Over HVDC*, Operations Reports, ENTSO-E, Brussels, Belgium, Feb. 2021. [Online]. Available: https://eepublicdownloads.entsoe.eu/clean-documents/SOC%20documents/Operational_Limits_and_Conditions_for_Mutual_Frequency_Support_over_HVDC_Report.pdf

[39] P. Kundur, "Definition and classification of power system stability IEEE/CIGRE joint task force on stability terms and definitions," *IEEE Trans. Power Syst.*, vol. 19, no. 3, pp. 1387–1401, May 2004, doi: 10.1109/TPWRS.2004.825981.

[40] S. Blumsack, "Frequency regulation," EBF 483: Introduction Electr. Markets, PennState, College Earth Mineral Sci., Univ. Park, Harrisburg, PA, USA, Tech. Rep. 9.1.2, 2021. [Online]. Available: https://www.e-education.psu.edu/ebf483/

[41] R. Salahshour, E. Mirmoradi, and H. Ghasemi, "EVs participation in energy and reserve market considering primary and tertiary frequency regulation constraints," in *Proc. Smart Grid Conf. (SGC)*, Dec. 2014, pp. 1–6, doi: 10.1109/SGC.2014.7151034.

[42] G. Zhang and J. McCalley, "Optimal power flow with primary and secondary frequency constraint," in *Proc. North Amer. Power Symp. (NAPS)*, Sep. 2014, pp. 1–6, doi: 10.1109/NAPS.2014.6965392.

[43] J. Morren, S. W. H. de Haan, W. L. Kling, and J. A. Ferreira, "Wind turbines emulating inertia and supporting primary frequency control," *IEEE Trans. Power Syst.*, vol. 21, no. 1, pp. 433–434, Feb. 2006, doi: 10.1109/TPWRS.2005.861956.

[44] J. F. Conroy and R. Watson, "Frequency response capability of full converter wind turbine generators in comparison to conventional generation," *IEEE Trans. Power Syst.*, vol. 23, no. 2, pp. 649–656, May 2008, doi: 10.1109/TPWRS.2008.920197.

[45] M. Dreidy, H. Mokhlis, and S. Mekhilef, "Inertia response and frequency control techniques for renewable energy sources: A review," *Renew. Sustain. Energy Rev.*, vol. 69, pp. 144–155, Mar. 2017, doi: 10.1016/j.rser.2016.11.170.

[46] H. Liu and Z. Chen, "Contribution of VSC-HVDC to frequency regulation of power systems with offshore wind generation," *IEEE Trans. Energy Convers.*, vol. 30, no. 3, pp. 918–926, Sep. 2015, doi: 10.1109/TEC.2015.2417130.

[47] G. Zhang, Z. Xu, and Y. Cai, "An equivalent model for simulating VSC based HVDC," in *Proc. IEEE/PES Transmiss. Distrib. Conf. Expo. Developing New Perspect.*, Nov. 2001, pp. 20–24, doi: 10.1109/TDC.2001.971203.

[48] Y. Pipelzadeh, B. Chaudhuri, and T. C. Green, "Inertial response from remote offshore wind farms connected through VSC-HVDC links: A communication-less scheme," in *Proc. IEEE Power Energy Soc. Gen. Meeting*, Jul. 2012, pp. 1–6, doi: 10.1109/PESGM.2012.6345609.

[49] S. Ray and G. K. Venayagamoorthy, "Real-time implementation of a measurement-based adaptive wide-area control system considering communication delays," *IET Gener. Transm. Distrib.*, vol. 2, no. 1, pp. 62–70, Jan. 2008, doi: 10.1049/iet-gtd:20070027.

[50] F. Wilches-Bernal, D. A. Schoenwald, R. Fan, M. Elizondo, and H. Kirkham, "Analysis of the effect of communication latencies on HVDC-based damping control," in *Proc. IEEE/PES Transmiss. Distrib. Conf. Expo. (T&D)*, Apr. 2018, pp. 1–9, doi: 10.1109/TDC.2018.8440146.

[51] T. M. Haileselassie, R. E. Torres-Olguin, T. K. Vrana, K. Uhlen, and T. Undeland, "Main grid frequency support strategy for VSC-HVDC connected wind farms with variable speed wind turbines," in *Proc. IEEE Trondheim PowerTech*, Jun. 2011, pp. 1–6, doi: 10.1109/PTC.2011.6019348.

[52] Y. Phulpin, "Communication-free inertia and frequency control for wind generators connected by an HVDC-link," *IEEE Trans. Power Syst.*, vol. 27, no. 2, pp. 1136–1137, May 2012, doi: 10.1109/TPWRS.2011.2175817.

[53] B. Silva, C. L. Moreira, L. Seca, Y. Phulpin, and J. A. P. Lopes, "Provision of inertial and primary frequency control services using offshore multi-terminal HVDC networks," *IEEE Trans. Sustain. Energy*, vol. 3, no. 4, pp. 800–808, Oct. 2012, doi: 10.1109/TSTE.2012.2199774.

[54] G.-L. Lu, C.-H. Lin, and Y.-K. Wu, "Comparison of communication-based and coordination-based frequency control schemes for HVdc-connected offshore wind farms," *IEEE Trans. Ind. Appl.*, vol. 57, no. 4, pp. 3352–3365, Aug. 2021, doi: 10.1109/TIA.2021.3079233.

[55] Z. Miao, L. Fan, D. Osborn, and S. Yuvarajan, "Wind farms with HVDC delivery in inertial response and primary frequency control," *IEEE Trans. Energy Convers.*, vol. 25, no. 4, pp. 1171–1178, Dec. 2010, doi: 10.1109/TEC.2010.2060202.

[56] Y. Li, Z. Zhang, Y. Yang, Y. Li, H. Chen, and Z. Xu, "Coordinated control of wind farm and VSC-HVDC system using capacitor energy and kinetic energy to improve inertia level of power systems," *Int. J. Elect. Power Energy Syst.*, vol. 59, pp. 79–92, Jul. 2014, doi: 10.1016/j.ijepes.2014.02.003.

[57] J. Zhu, C. D. Booth, G. P. Adam, A. J. Roscoe, and C. G. Bright, "Inertia emulation control strategy for VSC-HVDC transmission systems," *IEEE Trans. Power Syst.*, vol. 28, no. 2, pp. 1277–1287, May 2013, doi: 10.1109/TPWRS.2012.2213101.

[58] J. Zhu, H. Zhang, J. M. Guerrero, G. P. Adam, and C. D. Booth, "A generic inertia emulation controller for multi-terminal VSC-HVDC systems," in *Proc. 2nd IET Renew. Power Gener. Conf. (RPG)*, 2013, pp. 1–6, doi: 10.1049/cp.2013.1751.

[59] J. J. Grainger, W. D. Stevenson, and G. W. Chang, "Power system stability," in *Power System Analysis, International Edition*. New York, NY, USA: McGraw-Hill, 2016, pp. 528–550.

[60] A. Junyent-Ferr, Y. Pipelzadeh, and T. C. Green, "Blending HVDC-link energy storage and offshore wind turbine inertia for fast frequency response," *IEEE Trans. Sustain. Energy*, vol. 6, no. 3, pp. 1059–1066, Jul. 2015, doi: 10.1109/TSTE.2014.2360147.

[61] E. Ørum, *Future System Inertia*. Brussels, Belgium: ENTSO-E, Operations Reports, Sep. 2017. [Online]. Available: https://eepublicdownloads.entsoe.eu/clean-documents/Publications/SOC/Nordic/Nordic_report_Future_System_Inertia.pdf

[62] *Inertia and Rate of Change of Frequency (RoCoF)*, Operations Reports, Version, ENTSO-E, Brussels, Belgium, Dec. 2020. [Online]. Available: https://eepublicdownloads.azureedge.net/clean-documents/SOC%20documents/Inertia%20and%20RoCoF_v17_clean.pdf

[63] Y. Li, Z. Xu, J. Ostergaard, and D. J. Hill, "Coordinated control strategies for offshore wind farm integration via VSC-HVDC for system frequency support," *IEEE Trans. Energy Convers.*, vol. 32, no. 3, pp. 843–856, Sep. 2017, doi: 10.1109/TEC.2017.2663664.

[64] H. Alatrash, A. Mensah, E. Mark, G. Haddad, and J. Enslin, "Generator emulation controls for photovoltaic inverters," *IEEE Trans. Smart Grid*, vol. 3, no. 2, pp. 996–1011, Jun. 2012, doi: 10.1109/TSG.2012.2188916.

[65] X. Liu and A. Lindemann, "Control of VSC-HVDC connected offshore windfarms for providing synthetic inertia," *IEEE J. Emerg. Sel. Topics Power Electron.*, vol. 6, no. 3, pp. 1407–1417, Sep. 2018, doi: 10.1109/JESTPE.2017.2751541.

[66] S. J. Mason, "Feedback theory-further properties of signal flow graphs," *Proc. IRE*, vol. 44, no. 7, pp. 920–926, Jul. 1956, doi: 10.1109/JRPROC.1956.275147.

[67] Z. Lu, Y. Ye, and Y. Qiao, "An adaptive frequency regulation method with grid-friendly restoration for VSC-HVDC integrated offshore wind farms," *IEEE Trans. Power Syst.*, vol. 34, no. 5, pp. 3582–3593, Sep. 2019, doi: 10.1109/TPWRS.2019.2901986.

[68] J. Lee, E. Muljadi, P. Sorensen, and Y. C. Kang, "Releasable kinetic energy-based inertial control of a DFIG wind power plant," *IEEE Trans. Sustain. Energy*, vol. 7, no. 1, pp. 279–288, Jan. 2016, doi: 10.1109/TSTE.2015.2493165.

[69] A. R. A. Jerin, P. Kaliannan, and U. Subramaniam, "Improved fault ride through capability of DFIG based wind turbines using synchronous reference frame control based dynamic voltage restorer," *ISA Trans.*, vol. 70, pp. 465–474, Sep. 2017, doi: 10.1016/j.isatra.2017.06.029.

[70] V. Knap, R. Sinha, M. Swierczynski, D.-I. Stroe, and S. Chaudhary, "Grid inertial response with lithium-ion battery energy storage systems," in *Proc. IEEE 23rd Int. Symp. Ind. Electron. (ISIE)*, Jun. 2014, pp. 1817–1822, doi: 10.1109/ISIE.2014.6864891.

[71] U. Datta, A. Kalam, and J. Shi, "Battery energy storage system to stabilize transient voltage and frequency and enhance power export capability," *IEEE Trans. Power Syst.*, vol. 34, no. 3, pp. 1845–1857, May 2019, doi: 10.1109/TPWRS.2018.2879608.

[72] J. Liu, J. Wen, W. Yao, and Y. Long, "Solution to short-term frequency response of wind farms by using energy storage systems," *IET Renew. Power Gener.*, vol. 10, no. 5, pp. 669–678, May 2016, doi: 10.1049/iet-rpg.2015.0164.

[73] J. W. Choi, S. Y. Heo, and M. K. Kim, "Hybrid operation strategy of wind energy storage system for power grid frequency regulation," *IET Gener., Transmiss. Distrib.*, vol. 10, no. 3, pp. 736–749, Feb. 2016, doi: 10.1049/iet-gtd.2015.0149.

[74] F. Díaz-González, M. Hau, A. Sumper, and O. Gomis-Bellmunt, "Coordinated operation of wind turbines and flywheel storage for primary frequency control support," *Int. J. Electr. Power Energy Syst.*, vol. 68, pp. 313–326, Jun. 2015, doi: 10.1016/j.ijepes.2014.12.062.

[75] L. Qu and W. Qiao, "Constant power control of DFIG wind turbines with supercapacitor energy storage," *IEEE Trans. Ind. Appl.*, vol. 47, no. 1, pp. 359–367, Jan. 2011, doi: 10.1109/TIA.2010.2090932.

[76] N. S. Hasan, N. Rosmin, N. M. Nordin, and M. Y. Hassan, "Virtual inertial support extraction using a super-capacitor for a wind-PMSG application," *IET Renew. Power Gener.*, vol. 13, no. 10, pp. 1802–1808, Jul. 2019, doi: 10.1049/iet-rpg.2018.5655.

[77] M. I. Daoud, A. M. Massoud, A. S. Abdel-Khalik, A. Elserougi, and S. Ahmed, "A flywheel energy storage system for fault ride through support of grid-connected VSC HVDC-based offshore wind farms," *IEEE Trans. Power Syst.*, vol. 31, no. 3, pp. 1671–1680, May 2016, doi: 10.1109/TPWRS.2015.2465163.

[78] I. Ngamroo, "An optimization of superconducting coil installed in an HVDC-wind farm for alleviating power fluctuation and limiting fault current," *IEEE Trans. Appl. Supercond.*, vol. 29, no. 2, pp. 1–5, Mar. 2019, doi: 10.1109/TASC.2018.2881993.

[79] L. Wu, W. Gao, Z. Cui, and X. Kou, "A novel frequency regulation strategy with the application of energy storage system for large scale wind power integration," in *Proc. 7th Annu. IEEE Green Technol. Conf.*, Apr. 2015, pp. 221–226, doi: 10.1109/GREENTECH.2015.34.

[80] Z. Wu, D. W. Gao, H. Zhang, S. Yan, and X. Wang, "Coordinated control strategy of battery energy storage system and PMSG-WTG to enhance system frequency regulation capability," *IEEE Trans. Sustain. Energy*, vol. 8, no. 3, pp. 1330–1343, Jul. 2017, doi: 10.1109/TSTE.2017.2679716.

[81] L. Miao, J. Wen, H. Xie, C. Yue, and W.-J. Lee, "Coordinated control strategy of wind turbine generator and energy storage equipment for frequency support," *IEEE Trans. Ind. Appl.*, vol. 51, no. 4, pp. 2732–2742, Jul. 2015, doi: 10.1109/TIA.2015.2394435.

[82] M. N. Musarrat, M. R. Islam, K. M. Muttaqi, and D. Sutanto, "Enhanced frequency support from a PMSG-based wind energy conversion system integrated with a high temperature SMES in standalone power supply systems," *IEEE Trans. Appl. Supercond.*, vol. 29, no. 2, pp. 1–6, Mar. 2019, doi: 10.1109/TASC.2018.2882429.

[83] G. Delille, B. Francois, and G. Malarange, "Dynamic frequency control support by energy storage to reduce the impact of wind and solar generation on isolated power system's inertia," *IEEE Trans. Sustain. Energy*, vol. 3, no. 4, pp. 931–939, Oct. 2012, doi: 10.1109/TSTE.2012.2205025.

[84] N. Mendis, K. M. Muttaqi, and S. Perera, "Management of battery-supercapacitor hybrid energy storage and synchronous condenser for isolated operation of PMSG based variable-speed wind turbine generating systems," *IEEE Trans. Smart Grid*, vol. 5, no. 2, pp. 944–953, Mar. 2014, doi: 10.1109/TSG.2013.2287874.

[85] N. Mendis, K. M. Muttaqi, and S. Perera, "Management of low- and high-frequency power components in demand-generation fluctuations of a DFIG-based wind-dominated RAPS system using hybrid energy storage," *IEEE Trans. Ind. Appl.*, vol. 50, no. 3, pp. 2258–2268, May/Jun. 2014, doi: 10.1109/TIA.2013.2289973.

[86] Y. Tan, K. M. Muttaqi, P. Ciufo, L. Meegahapola, X. Guo, B. Chen, and H. Chen, "Enhanced frequency regulation using multilevel energy storage in remote area power supply systems," *IEEE Trans. Power Syst.*, vol. 34, no. 1, pp. 163–170, Jan. 2019, doi: 10.1109/TPWRS.2018.2867190.

[87] J. Dang, J. Seuss, L. Suneja, and R. G. Harley, "SoC feedback control for wind and ESS hybrid power system frequency regulation," *IEEE J. Emerg. Sel. Topics Power Electron.*, vol. 2, no. 1, pp. 79–86, Mar. 2014, doi: 10.1109/jestpe.2013.2289991.

[88] X. Li, Y. Huang, J. Huang, S. Tan, M. Wang, T. Xu, and X. Cheng, "Modeling and control strategy of battery energy storage system for primary frequency regulation," in *Proc. Int. Conf. Power Syst. Technol.*, Oct. 2014, pp. 543–549, doi: 10.1109/POWERCON.2014.6993760.

[89] X. Lu, K. Sun, J. M. Guerrero, J. C. Vasquez, L. Huang, and R. Teodorescu, "SoC-based droop method for distributed energy storage in DC microgrid applications," in *Proc. IEEE Int. Symp. Ind. Electron.*, May 2012, pp. 1640–1645, doi: 10.1109/ISIE.2012.6237336.

[90] E. Thorbergsson, V. Knap, M. Swierczynski, D. Stroe, and R. Teodorescu, "Primary frequency regulation with Li-ion battery based energy storage system–evaluation and comparison of different control strategies," in *Proc. Intelec 35th Int. Telecommun. Energy Conf., Smart Power Efficiency*, Oct. 2013, pp. 1–6.

[91] V. Knap, S. K. Chaudhary, D.-I. Stroe, M. Swierczynski, B.-I. Craciun, and R. Teodorescu, "Sizing of an energy storage system for grid inertial response and primary frequency reserve," *IEEE Trans. Power Syst.*, vol. 31, no. 5, pp. 3447–3456, Sep. 2016, doi: 10.1109/TPWRS.2015.2503565.

[92] M. S. Akbari, A. A. Safavi, N. Vafamand, T. Dragicevic, and J. Rodriguez, "Fuzzy mamdani-based model predictive load frequency control," in *Proc. IEEE 11th Int. Symp. Power Electron. Distrib. Gener. Syst. (PEDG)*, Sep. 2020, pp. 7–12, doi: 10.1109/PEDG48541.2020.9244311.

[93] I. E. Uyioghosa and A. K. Saha, "Adaptive model predictive control for frequency control for two area interconnected power system," in *Proc. Southern Afr. Universities Power Eng. Conf./Robotics Mechatronics/Pattern Recognit. Assoc. South Afr. (SAUPEC/RobMech/PRASA)*, Jan. 2021, pp. 1–6, doi: 10.1109/SAUPEC/RobMech/PRASA52254.2021.9377021.

[94] Y. Liu, Y. Chen, and M. Li, "Dynamic event-based model predictive load frequency control for power systems under cyber attacks," *IEEE Trans. Smart Grid*, vol. 12, no. 1, pp. 715–725, Jan. 2021, doi: 10.1109/TSG.2020.3022094.

[95] H. H. Ali, A. M. Kassem, M. Al-Dhaifallah, and A. Fathy, "Multi-verse optimizer for model predictive load frequency control of hybrid multi-interconnected plants comprising renewable energy," *IEEE Access*, vol. 8, pp. 114623–114642, 2020, doi: 10.1109/ACCESS.2020.3004299.

[96] A. Oshnoei, M. Kheradmandi, and S. M. Muyeen, "Robust control scheme for distributed battery energy storage systems in load frequency control," *IEEE Trans. Power Syst.*, vol. 35, no. 6, pp. 4781–4791, Nov. 2020, doi: 10.1109/TPWRS.2020.2997950.

[97] N. Sockeel, J. Gafford, B. Papari, and M. Mazzola, "Virtual inertia emulator-based model predictive control for grid frequency regulation considering high penetration of inverter-based energy storage system," *IEEE Trans. Sustain. Energy*, vol. 11, no. 4, pp. 2932–2939, Oct. 2020, doi: 10.1109/TSTE.2020.2982348.

[98] R. K. Subroto, K. L. Lian, C.-C. Chu, and C.-J. Liao, "A fast frequency control based on model predictive control taking into account of optimal allocation of power from the energy storage system," *IEEE Trans. Power Del.*, vol. 36, no. 4, pp. 2467–2478, Aug. 2021, doi: 10.1109/TPWRD.2021.3078217.

[99] A. S. Hussein, N. H. El-Amary, A. Y. Abdelaziz, and R. A. Swief, "Model predictive control for hybrid AC/DC micro-grids," in *Proc. Int. Conf. Innov. Trends Commun. Comput. Eng. (ITCE)*, Feb. 2020, pp. 365–369, doi: 10.1109/ITCE48509.2020.9047785.

[100] J. Zhang, X. Shao, Y. Li, J. Lin, F. Li, and Z. Zhang, "Research on frequency regulation strategy based on model predictive control for wind-hydro-storage complementary microgrid," in *Proc. 4th Int. Conf. HVDC (HVDC)*, Nov. 2020, pp. 1031–1036, doi: 10.1109/HVDC50696.2020.9292853.

[101] M. U. Jan, A. Xin, H. U. Rehman, M. A. Abdelbaky, S. Iqbal, and M. Aurangzeb, "Frequency regulation of an isolated microgrid with electric vehicles and energy storage system integration using adaptive and model predictive controllers," *IEEE Access*, vol. 9, pp. 14958–14970, 2021, doi: 10.1109/ACCESS.2021.3052797.

[102] P. M. Namara, A. Ortega, and F. Milano, "Model predictive control based AGC for multi-terminal DC grids," in *Proc. IEEE Power Energy Soc. Gen. Meeting (PESGM)*, Jul. 2016, pp. 1–5, doi: 10.1109/PESGM.2016.7741354.

[103] P. Mc Namara, R. R. Negenborn, B. De Schutter, G. Lightbody, and S. McLoone, "Distributed MPC for frequency regulation in multi-terminal HVDC grids," *Control Eng. Pract.*, vol. 46, pp. 176–187, Jan. 2016, doi: 10.1016/j.conengprac.2015.11.001.

[104] P. McNamara and F. Milano, "MPC based AGC for AC/DC grids with delays and voltage constraints," in *Proc. IEEE Power Energy Soc. Gen. Meeting*, Jul. 2017, pp. 1–5, doi: 10.1109/PESGM.2017.8274515.

[105] P. McNamara and F. Milano, "Model predictive control-based AGC for multi-terminal HVDC-connected AC grids," *IEEE Trans. Power Syst.*, vol. 33, no. 1, pp. 1036–1048, Jan. 2018, doi: 10.1109/TPWRS.2017.2694768.

[106] H. Ye, W. Pei, L. Kong, and T. An, "Low-order response modeling for wind farm-MTDC participating in primary frequency controls," *IEEE Trans. Power Syst.*, vol. 34, no. 2, pp. 942–952, Mar. 2019, doi: 10.1109/TPWRS.2018.2874042.

[107] O. Gomis-Bellmunt, A. Junyent-Ferre, A. Sumper, and J. Bergas-Jane, "Control of a wind farm based on synchronous generators with a central HVDC-VSC converter," *IEEE Trans. Power Syst.*, vol. 26, no. 3, pp. 1632–1640, Aug. 2011, doi: 10.1109/TPWRS.2010.2091654.

[108] M. Ndreko, J. L. Rueda, M. Popov, and M. A. M. M. van der Meijden, "Optimal fault ride through compliance of offshore wind power plants with VSC-HVDC connection by meta-heuristic based tuning," *Electr. Power Syst. Res.*, vol. 145, pp. 99–111, Apr. 2017, doi: 10.1016/j.epsr.2016.12.024.

[109] W. Wang, Y. Li, Y. Cao, U. Häger, and C. Rehtanz, "Adaptive droop control of VSC-MTDC system for frequency support and power sharing," *IEEE Trans. Power Syst.*, vol. 33, no. 2, pp. 1264–1274, Mar. 2018, doi: 10.1109/TPWRS.2017.2719002.

[110] M. Tavakoli, E. Pouresmaeil, J. Adabi, R. Godina, and J. P. S. Catalão, "Load-frequency control in a multi-source power system connected to wind farms through multi terminal HVDC systems," *Comput. Oper. Res.*, vol. 96, pp. 305–315, Aug. 2018, doi: 10.1016/j.cor.2018.03.002.

[111] A. O. Aluko, D. G. Dorrell, R. P. Carpanen, and E. E. Ojo, "Heuristic optimization of virtual inertia control in grid-connected wind energy conversion systems for frequency support in a restructured environment," *Energies*, vol. 13, no. 3, p. 564, Jan. 2020.

[112] Q. Ai, T. Liu, Y. Yin, and Y. Tao, "Frequency coordinated control strategy of HVDC sending system with wind power based on situation awareness," *IET Gener. Transm. Distrib.*, vol. 14, no. 16, pp. 3179–3186, 2020, doi: 10.1049/iet-gtd.2020.0204.

[113] J. Z. Zhou, H. Ding, S. Fan, Y. Zhang, and A. M. Gole, "Impact of short-circuit ratio and phase-locked-loop parameters on the small-signal behavior of a VSC-HVDC converter," *IEEE Trans. Power Del.*, vol. 29, no. 5, pp. 2287–2296, Oct. 2014, doi: 10.1109/TPWRD.2014.2330518.

[114] Y. Liu, M. Hao, Y. He, C. Zang, and P. Zeng, "Review and applications of virtual synchronous machines technologies," in *Proc. IEEE Innov. Smart Grid Technol. Asia (ISGT Asia)*, May 2019, pp. 593–598, doi: 10.1109/ISGT-Asia.2019.8881466.

[115] B. Li, L. Zhou, X. Yu, C. Zheng, and J. Liu, "Improved power decoupling control strategy based on virtual synchronous generator," *IET Power Electron.*, vol. 10, no. 4, pp. 462–470, Mar. 2017, doi: 10.1049/iet-pel.2016.0608.

[116] J. Guo, Y. Chen, S. Liao, W. Wu, L. Zhou, Z. Xie, and X. Wang, "Analysis and mitigation of low-frequency interactions between the source and load virtual synchronous machine in an islanded microgrid," *IEEE Trans. Ind. Electron.*, early access, May 3, 2021, doi: 10.1109/TIE.2021.3075847.

[117] J. Liu, Y. Miura, and T. Ise, "Comparison of dynamic characteristics between virtual synchronous generator and droop control in inverter-based distributed generators," *IEEE Trans. Power Electron.*, vol. 31, no. 5, pp. 3600–3611, May 2016, doi: 10.1109/TPEL.2015.2465852.

[118] Y. Wang, L. Luo, T. Li, Y. Chen, and Y. Fu, "Research on control strategy of improved virtual synchronous generator for improving the operating capability of passive isolated islands," in *Proc. IEEE Innov. Smart Grid Technol. Asia (ISGT Asia)*, May 2019, pp. 1485–1490, doi: 10.1109/ISGT-Asia.2019.8881448.

[119] H. Zhang, D. Yang, Y. Mu, B. Wen, X. Li, and X. N. Yang, "A combination control strategy of VSC-HVDC with wind farms based on virtual synchronous generator of voltage drop method," in *Proc. China Int. Conf. Electr. Distrib. (CICED)*, Sep. 2018, pp. 1604–1610, doi: 10.1109/CICED.2018.8592438.

[120] J. Jia, Y. Yang, and K. Ji, "Unbalanced voltage improvement control of virtual synchronous rectifier," in *Proc. IEEE 8th Annu. Int. Conf. CYBER Technol. Autom., Control, Intell. Syst. (CYBER)*, Jul. 2018, pp. 1171–1176, doi: 10.1109/CYBER.2018.8688317.

[121] J. Xu, X. Cao, and Z. Hao, "A droop control strategy based on synchronous rectifier to modulate the frequency and voltage in AC microgrid," in *Proc. 22nd Int. Conf. Electr. Mach. Syst. (ICEMS)*, Aug. 2019, pp. 1–5, doi: 10.1109/ICEMS.2019.8921702.

[122] Q.-C. Zhong and G. Weiss, "Synchronverters: Inverters that mimic synchronous generators," *IEEE Trans. Ind. Electron.*, vol. 58, no. 4, pp. 1259–1267, Apr. 2011, doi: 10.1109/TIE.2010.2048839.

[123] C. Andalib-Bin-Karim, X. Liang, and H. Zhang, "Fuzzy-secondary-controller-based virtual synchronous generator control scheme for interfacing inverters of renewable distributed generation in microgrids," *IEEE Trans. Ind. Appl.*, vol. 54, no. 2, pp. 1047–1061, Apr. 2018, doi: 10.1109/TIA.2017.2773432.,

[124] M. Guan, W. Pan, J. Zhang, Q. Hao, J. Cheng, and X. Zheng, "Synchronous generator emulation control strategy for voltage source converter (VSC) stations," *IEEE Trans. Power Syst.*, vol. 30, no. 6, pp. 3093–3101, Nov. 2015, doi: 10.1109/TPWRS.2014.2384498.

[125] L. M. Castro and E. Acha, "On the provision of frequency regulation in low inertia AC grids using HVDC systems," *IEEE Trans. Smart Grid*, vol. 7, no. 6, pp. 2680–2690, Nov. 2016, doi: 10.1109/TSG.2015.2495243.

[126] L. Huang, H. Xin, H. Yang, Z. Wang, and H. Xie, "Interconnecting very weak AC systems by multiterminal VSC-HVDC links with a unified virtual synchronous control," *IEEE J. Emerg. Sel. Topics Power Electron.*, vol. 6, no. 3, pp. 1041–1053, Sep. 2018, doi: 10.1109/JESTPE.2018.2825391.

[127] X. Wu, J. Mei, B. Wang, D. Liang, C. Qin, and J. Zong, "Unbalanced loads control strategy for virtual synchronous generator in passive network," in *Proc. IEEE Innov. Smart Grid Technol. Asia (ISGT Asia)*, May 2019, pp. 2063–2068, doi: 10.1109/ISGT-Asia.2019.8881184.

[128] J. Guo, Y. Chen, S. Liao, W. Wu, X. Wang, and J. M. Guerrero, "Low-frequency oscillation analysis of VSMs-based VSC-HVDC systems based on the five-dimension impedance stability criterion," *IEEE Trans. Ind. Electron.*, early access, May 5, 2021, doi: 10.1109/TIE.2021.3076711.

[129] F. Wang, L. Zhang, X. Feng, and H. Guo, "An adaptive control strategy for virtual synchronous generator," *IEEE Trans. Ind Appl.*, vol. 54, no. 5, pp. 5124–5133, Sep./Oct. 2018, doi: 10.1109/TIA.2018.2859384.

CHUNG-HAN LIN was born in Pingtung, Taiwan, in 1999. He received the B.S. degree in electrical engineering from the National Chung Cheng University, Chiayi, Taiwan, where he is currently pursuing the M.S. degree. His research interests include the wind turbine models and the frequency control strategies for VSC-HVDC, wind farm, and energy storage systems.

YUAN-KANG WU (Member, IEEE) received the Ph.D. degree in electronic and electrical engineering from the University of Strathclyde, Glasgow, U.K., in 2004. He was a Researcher with the Industrial Technology Research Institute (ITRI), Hsinchu, Taiwan, and an Engineer with Taiwan Electric Research and Testing Center (TERTEC), Taiwan. He is currently a Professor with the Department of Electrical Engineering, National Chung-Cheng University, Chiayi, Taiwan, working in the area of wind turbine modeling, wind and solar power systems, offshore wind farm planning, renewable energy forecasting techniques, power system control and management, distributed generation, and smart grid control.